DEVELOPMENT OF AN OPTICAL ROTARY INTERFACE USING RADIAL LIGHT FROM AN EMISSIVE OPTICAL FIBER

Codey Heinz Nacke

Department of Electrical Engineering
McGill University, Montreal

Submitted January, 2023

A thesis submitted to McGill University in partial fulfillment of the requirements of the degree of Masters of Science.

Contents

Abstract

Using the radially radiated light from an emissive optical fiber, high speed communication across an orbital interface is shown with reduced complexity and size when compared to current solutions. Data rates at over 1 Gbit/s with a BER of 2.7×10^{-3} are achieved with direct LED modulation at a single wavelength with adaptive bit and power loading real-valued OFDM. A simulation architecture for emissive optical fibers is developed using non-sequential raytracing methods and validated using experimental results and analytical modeling. The system parameters are characterized, and rapid prototyping is demonstrated. By utilizing an elliptical reflector, an increase of 1.77 dBm of detected power is achieved in simulation with a simultaneous reduction in the system's footprint and complexity.

Résumé

En utilisant la lumière rayonnée radialement par une fibre optique émissive, la communication rapide à travers une interface orbitale est démontrée avec une complexité et une taille réduite par rapport aux solutions actuelles. Des débits de données excédant 1 Gbit/s avec un BER de 2.7×10^{-3} sont atteints avec une modulation directe par LED à une seule longueur d'onde avec l'OFDM à valeur réelle à chargement adaptatif de bits et de puissance. Une architecture de simulation pour les fibres optiques émissives est développée en utilisant des méthodes de lancer de rayons non séquentiel et validée à l'aide de résultats expérimentaux et d'une modélisation analytique. Les paramètres du système sont caractérisés, et un prototypage rapide est démontré. En utilisant un réflecteur elliptique, une augmentation de 1.77 dBm de la puissance détectée est obtenue en simulation avec une réduction simultanée de la complexité et de la taille du système.

Acknowledgements

Sincere thanks to Prof. David Plant, and Prof. Lawrence Chen for their continued guidance on this project, and a special thanks to Zixian Wei, Mostafa Khalil, Amna Riaz, and Hao Sun for their help throughout this project. I must also thank Kyle Stitt and James Lougheed from Ottawa for bringing this project to us and the incredible collaboration it has provided.

Finally a thanks to CMC Microsystems for lending us RTOs, and to Keysight for providing an AWG. Without this critical equipment was used throughout the project and much could not have been done without it.

Contribution of Authors

Guidance and feedback has been provided by Prof. David Plant, Prof. Lawrence Chen , Zixian Wei, Amna Riaz, Mostafa Khalil, and Hao Sun from McGill University, and Kyle Stitt and James Lougheed from Ottawa for the duration of the project and thesis preparation.

Part I

The vast majority of the code written for this project is my own. I am responsible for collecting all the data presented. In some instances, assistance was provided in writing the code by Mostafa Khalil, Hao Sun, and Zixian Wei. Mostafa Khalil and Zixian Wei also provided assistance during data collection on several occasions. The demonstrator unit was provided by Kyocera SLD, additional experimental setups were conceived and constructed by me.

Part II

The simulations and associated code is entirely my own work. The experimental setups were conceived and constructed by me. Assistance in acquiring the experimental data was provided by Amna Riaz and Zixian Wei on several occasions.

List of Figures

List of Tables

Acronyms

AWG arbitrary waveform generator 4, 10

BER bit error rate 2, 7–9, 12, 16–19, 72

CFO carrier frequency offset 5, 6, 15–18, 77

CP cyclic prefix 4

CPE common phase error 5, 6, 15–17, 77

CWL central wavelength 21, 24

FC/APC fiber-optic connector/angled physical contact 22, 31, 51, 52

FFT fast fourier tansform 4

FWHM full-width half-maximum 21, 24

IFFT inverse fast fourier tansform 4, 10

IR infrared ..... viii, ix, 21, 22, 24, 31, 40, 47, 51–55, 57–60

ISI inter-symbol interference 4

NSRT non-sequential ray tracing 25, 26

OFDM orthogonal frequency domain multiplexing 2–4, 7, 12, 13, 17

OWC optical wireless communication xii

PAPR peak to average power ratio 4

QAM quadrature amplitude modulation 2–5, 7, 8, 10, 12, 13, 16, 19, 77

RF radio frequency ..... xii, 22

RMSE root-mean-square error 52

RTO real-time oscilloscope 4, 10

Rx receiver 10

SNR signal-to-noise ratio 7–9, 12, 13, 18, 19, 72, 77, 78

SRT sequential ray tracing 25, 26

Tx transmitter 10, 21

VLC visible light communication xii

Introduction

Optical wireless communications (OWCs) has been gaining popularity in recent times with the advancement of fields such as visible light communication (VLC) for use in Li-Fi technology. OWC has many befits over traditional wireless radio frequency (RF) communications, namely higher data rates, a larger available spectrum, and no electromagnetic interference [1]. The proponents of Li-Fi hope to use modulated LED lights to transmit data, because of this, advancements have been made using diffuse optical sources to transmit data with non-imaging optical systems. These advancements open the door for other OWCs in in more specialized applications.

Here we investigate the use of a VLC system for use in a large diameter optical rotary interface. Rotary interfaces are devices which allow signals to be transmitted between two continuously rotating sections. Electrical rotary interfaces are more commonly used in-place of optical interfaces because of their reduced cost and complexity. If the application permits, wireless RF communications can also be used for even greater simplicity. Where these alternatives fail is in cases where the data rate needed is too high. The Wi-Fi 6 standards is capable of 9.6 Gbit/s while single channel electronic rotary interfaces are capable of 5 Gbit/s, in contrast, single channel optical rotary interfaces care capable of 10 Gbit/s [2][3]. Electronic and RF alternatives are also susceptible to electromagnetic interference whereas optical systems are not. This makes optical rotary joints ideal for applications such as CT scans where large magnetic fields are used by the machine and large data rates are needed to transfer the acquired information.

The challenge with large diameter rotary interfaces is that the rotation center must remain free. This means that the transmission must take place along the perimeter of the ring which requires that a continuous signal between two moving targets is maintained.

Current solutions use a series of lasers and an array of collection optics. The number of lasers and size of the collection array are chosen so that there is always at least one laser hitting once of the collection devices, Figure. 1a. This means that either a large number of sources need to be places around the perimeter or that a large array of collecting optics are needed, or both.

The proposed solution utilizes an emissive optical fiber placed around the perimeter of one of the rings, Figure. 1b This creates a continuous source whose signal will not be interrupted as the interface rotates. As few as a single detector could be used for the entire data ring. In addition, less complex optics means that it is likely that a large spectrum of light can be used to transmit data, this implied more multiplexed channels and an larger combined data rate over a single optical fiber. Fewer components are also idea from a durability, reliability, maintenance, and cost perspective.

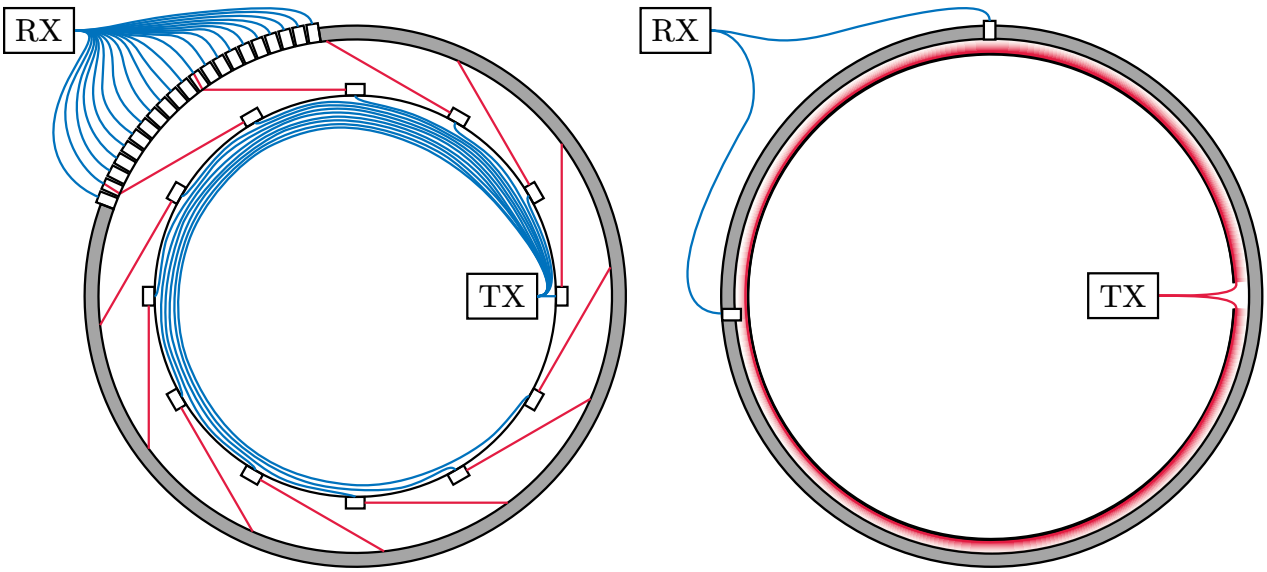

(a) Moog [3] (b) Emissive fiber

Figure 1: Comparison of large diameter optical rotary interfaces.

Challenges of the emissive fiber based optical rotary interface are the low amount of detected power and the resulting signal processing needed to maximize the channel throughput. As an optical fiber will radiate from its entire surface, the irradiance of the fiber is low

compared to laser based systems such as the one in Figure. 1a.

As the fiber is a diffuse source it will form toroidal iso-intensity surfaces of radiated light with surface area given by $4\pi^2 Rr$, where R is the distance from the center of the fiber ring to the center of the fiber, and r is the radius of the fiber. As an example, a 1 m diameter data ring with a fiber radius of 1 mm will have a fiber surface area of 197 cm^2. A distance of 1 cm between the fiber center and the detector thus results in a drop in irradiance by a multiple of 10 as the irradiance drops linearly with the radial distance from the fiber.

Finally, the diffuse radiation from the fiber means light incident on the detector will be coming from a wider range of directions and locations. This will result in less detected light as various components have limited acceptance angles. This may also effect the coherence bandwidth as the multiple optical paths between the fiber and detector will result in a spread of phases in the optical signal.

The objective of this project is to optimize the performance of the optical rotary interface. In Part I, signal modulation and processing techniques are tested on a demonstrator unit by Kyocera SLD as a proof of concept and verification of core concepts. In Part II, a simulation framework for emissive fiber systems is developed to further characterize the parameter space and to enable additional rapid prototyping. Combined, the two parts are intended to demonstrate current capabilities of a potential emissive fiber based optical rotary interface, to provide effective tools for understanding and improving those capabilities, and to showcase a selection of future development paths.

Part I

Signal Processing

Methods

Signal processing techniques are utilized to demonstrate the performance of the demonstrator unit. The unit can transmit over a broadband optical frequency spectrum. This invites the use of orthogonal frequency domain multiplexing (OFDM) which is a multi-carrier modulation format that has high spectral efficiency [4][5]. However, as the transmitter uses direct modulation, the system is limited to real-valued waveforms [6].

1.1 Real Valued OFDM

OFDM is a technique where a frequency spectrum is divided into a number of independent subcarriers, each capable of transmitting a unique signal. The subcarriers can each be modulated to increase the data rate of the signal. The most common modulation technique for OFDM is quadrature amplitude modulation (QAM), where a signal is given a complex and imaginary component, usually encoded in the power and phase components of the physical signal. Complex QAM data results in a complex OFDM signal, however, the optical signal used in the optical rotary joint is from a diffuse source, as such it is incoherent and does not have a recoverable phase component. This means that the signal is real-values and thus real-valued OFDM is required to encode the signal.

Real-valued OFDM is enabled by requiring that the data has Hermitian symmetry [7]. This is accomplished by requiring that the complex conjugate of the data is mirrored about the zero frequency subcarrier. This is akin to using half of the waveform information capacity for the real valued component of the data and the other half for the imaginary component.

In Figure. 1.1, the simplified process for creating an OFDM symbol is outlined. The input binary data is modulated using QAM, the number of bits per QAM symbol, and thus per subcarrier, is variable and depends on the channel capacity and acceptable bit error rate (BER). Pilot values are interleaved with the QAM data then assigned to a selection of

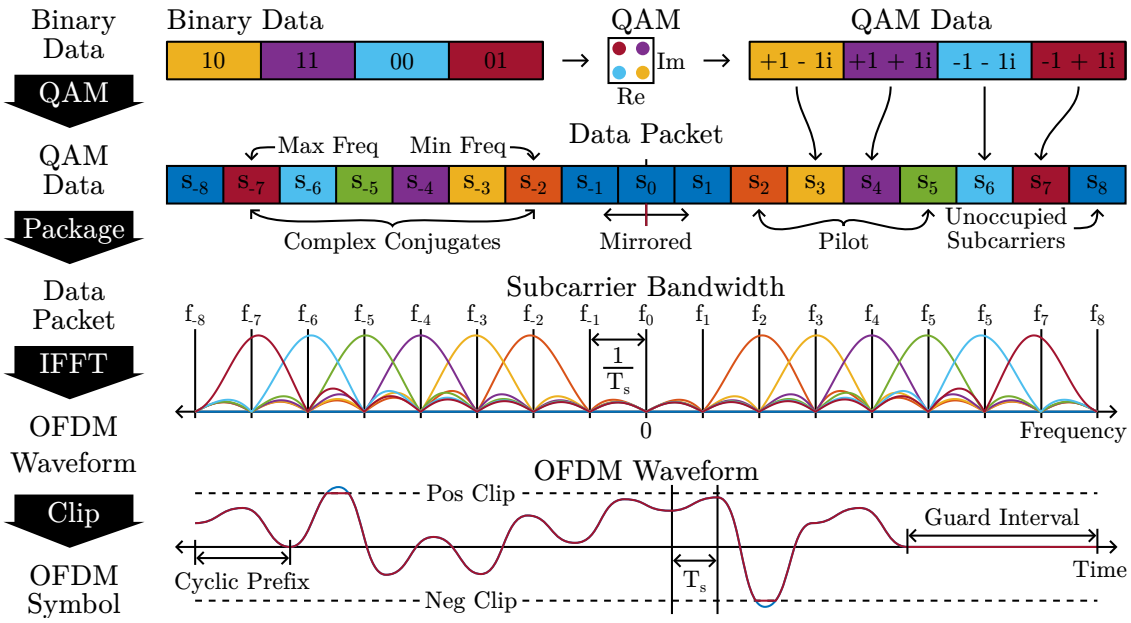

Figure 1.1: Real valued OFDM implementation. Binary data is QAM encoded, a pilot is added, and the then assigned to the positive frequency subcarriers. The complex conjugate is then mirrored into the negative frequency subcarriers to complete the data packet. The IFFT can then be taken to generate the OFDM waveform which is then clipped and a cyclic prefix and guard interval added to make the final OFDM symbol.

positive frequency subcarriers with the complex conjugate of the QAM data getting assigned to the mirrored negative subcarriers. This ensures that the Hermitian symmetry condition is met.

The total number of subcarriers is determined by the number of samples N_s in the final OFDM symbol. The individual subcarrier bandwidth B_n is dependent on the sample rate R_s which is the inverse of the sample time T_s. The total theoretical bandwidth B of the OFDM symbol is determined by the number of subcarriers and the individual subcarrier bandwidth. If the sample rate is fixed, for example because of an equipment limitation, the QAM data can be padded with unoccupied subcarriers to limit the utilized OFDM bandwidth.

$$R_s = \frac{1}{T_s} \tag{1.1}$$

$$B = N_s B_n = N_s R_s = N_s / T_s \tag{1.2}$$

With subcarriers assigned, the inverse fast fourier tansform (IFFT) can be taken to produce the OFDM waveform. To allow for circular convolution and easier frequency offset correction on the receiver side, a cyclic prefix (CP) is added, then to reduce the peak to average power ratio (PAPR), the waveform is clipped [8][9]. Finally a guard interval is appended to the end of the waveform to reduce the inter-symbol interference (ISI), this completes the OFDM symbol. The symbol then undergoes digital to analog conversion via arbitrary waveform generator (AWG) and electro-optic conversion via the optical source.

On the receiver side, the symbol undergoes opto-electric conversion in the detector and is converted from analog to digital using an analog-to-digital converter, in this experiment this is done via a real-time oscilloscope (RTO). The waveform start can then be detected by the guard interval and the CP, and the fast fourier tansform (FFT) taken to retrieve the data packet. The pilots can then be used to produce a pilot assisted channel estimation which is applied to the QAM data. Finally the QAM data is demodulated to recover the transmitted binary data.

1.1.1 Clipping

The PAPR is a useful metric for determining if there are large spikes in the OFDM waveform. As both the output level of the AWG and the range of acceptable signal potentials in the electro-optic conversion are limited, the waveform amplitude range must be normalized to an appropriate level. Short spikes in the waveform reduce the mean dynamic range of the waveform and suppress overall performance. By clipping the waveform, the mean dynamic range and PAPR are improved. The clipping value is determined relative to the distribution of waveform values and subsequent standard deviation.

1.1.2 Channel Estimation

Channel estimation is a vital step in recovering the transmitted data. Through a variety of methods, the effect of the channel is estimated

1.1.2.1 Pilot Assisted

The pilot assisted channel estimation is performed by comparing the known output pilot subcarrier data D'_{out} with the known input pilot subcarrier data D'_{in}. The correction is performed in two steps, the first step estimates and corrects for the common phase error (CPE) which makes the second step, where the carrier frequency offset (CFO) is corrected, perform better.

CPE can arise from a mismatch between the transmitter and receiver clocks and manifests as a subcarrier dependent rotation of the QAM data about the complex plane origin. The QAM modulated data is described in polar coordinates by its distance from the origin r and its phase ψ

$$D' = re^{i\psi} \tag{1.3}$$

The phase difference $\Delta\psi' = \psi'_{\text{out}} - \psi'_{\text{in}}$ of each pilot is computed via the pilot transfer function H'.

$$H' = D'_{\text{out}}/D'_{\text{in}} = (r'_{\text{out}}/r'_{\text{in}})\, e^{i\Delta\psi'} \tag{1.4}$$

A linear fit $\mathcal{P}$ is applied to the relation between $\Delta\psi'$ and subcarrier frequency ω. The relative difference between subsequent subcarrier phase is required, thus $\Delta\psi'$ must be unwrapped prior to fitting.

$$\mathcal{P}(\omega) = \phi\omega + c \tag{1.5}$$

The fitted slope ϕ is then used in Equation. 1.6 and Equation. 1.7 to compute the CPE compensated pilot data D'_{CPE} and the full CPE compensated data D_{CPE} respectively.

$$D'_{\text{CPE}} = D'_{\text{out}} i e^{i\omega\phi} \tag{1.6}$$

$$D_{\mathrm{CPE}} = D_{\mathrm{out}} i e^{i\omega\phi} \tag{1.7}$$

In the second step, the CFO of the CPE corrected data is estimated using an updated transfer function for the CPE corrected pilots H'_{CPE}.

$$H'_{\mathrm{CPE}} = D'_{\mathrm{CPE}} / D'_{\mathrm{in}} \tag{1.8}$$

A polynomial fit $\mathcal{H}$ is performed on H'_{CPE} and used to estimate the channel effect for all subcarriers.

$$\mathcal{H}(\omega) = \sum_{m=0}^{M} \beta_m \omega^m \tag{1.9}$$

Where β_m is the fit parameter of order m, and M is the degree of the polynomial fit. Depending on the complexity of the channel and if other pre-processing techniques are used, such as a training symbol assisted channel estimation, polynomial fits of degree $M = 3$ to $M = 11$ are used.

$$D'_{\mathrm{CFO}} = D'_{\mathrm{CPE}} / \mathcal{H} \tag{1.10}$$

$$D_{\mathrm{CFO}} = D_{\mathrm{CPE}} / \mathcal{H} \tag{1.11}$$

The CFO correction can be used without the CPE correction as the polynomial fit can correct for the CPE. However, testing found that removing the linear phase error prior to performing the CFO correction resulted in a better CFO fit.

1.1.2.2 Training Symbol Assisted

In addition to the pilot assisted channel estimation, a channel training set can be compiled either by transmitting known training symbols or by using the pilot information from a large number of symbols. The average path effects can then be determined from a larger data set to

produce a more accurate correction. The aggregate channel correction is thus applied before the pilot assisted channel estimation to remove the mean error and then further corrected with pilots.

As implemented, the training symbol assisted channel estimation is determined by transmitting a larger number of OFDM symbols with known data. The transfer function is then computed for each OFDM symbol and the transfer function from all the training symbols is averaged.

$$\mathbf{H} = \text{mean}\,(H_n) \tag{1.12}$$

The transmitted data is then corrected by dividing by the aggregate transfer function $\mathbf{H}$ to produce the training symbol corrected data D_{tsa}.

$$D_{\text{tsa}} = D_{\text{out}}/\mathbf{H} \tag{1.13}$$

D_{tsa} can then be substituted for D_{out} in Section. 1.1.2.1 to improve the system performance.

1.1.3 Adaptive Bit and Power Loading

As the transceiver's frequency response is not flat, the signal-to-noise ratio (SNR) is not uniform across all subcarriers. To maximize the system performance, the capacity of each subcarrier can be tuned to its individual SNR, this is called adaptive bit and power loading.

Adaptive bit loading is accomplished by having the subcarriers QAM order be variable. A subcarrier with a high SNR can accommodate a higher QAM order than a subcarrier with a low SNR for the same BER. Adaptive power loading is accomplished by allocating different amount of power to each subcarrier which in turn effects the subcarrier SNR. Adaptive power loading is used in conjunction with adaptive bit loading to balance the subcarriers' SNRs in a way that maximized the channel's efficiency.

Having an estimation of the channel's SNR versus frequency is required for adaptive bit

and power loading. This is can be accomplished via the channel training and estimation methods outlined in Section. 1.1.2, by utilizing forward error correction to estimate subcarrier BERs, and other methods or a combination of these methods. Here only channel training is utilized for its simplicity.

The Levin-Campello algorithm is used to determine the number of bits and amount of relative power to assign to each subcarrier. The algorithm is known as a water filling algorithm as it fills the subcarriers one-by-one keeping the SNR constant across all subcarriers.

1.1.3.1 Adaptive Bit Loading

To determine maximum QAM order that a subcarrier is capable of transmitting at a target BER, the relationship between SNR and BER must be known for every potential QAM order [10][11]. This allows the SNR gap, Γ_n, between different QAM orders to be determined. The SNR gap is used to estimate the required SNR, $r\text{SNR}(\bar{b}_n)$, needed for the n^{th} subcarrier to transmit $\bar{b}_n$ bits.

$$\bar{b}_n = \log_2\left(1 + |g_n|^2 \frac{\text{SNR}[n]}{\Gamma_n}\right) \tag{1.14}$$

$$\Gamma_n = \frac{r\text{SNR}(\bar{b}_n)}{2^{\bar{b}_n} - 1} \tag{1.15}$$

Where g_n is the subcarrier gain factor and $\bar{b}_n$ is the maximum achievable capacity of a subcarrier for the given modulation format and target BER. For a real system, the SNR is estimated and as such it is usually preferable to transmit $b_n \leq \bar{b}_n$ bits to ensure that the BER is below the target BER. We then define the SNR margin, $\lambda_n \geq 1$, as the difference between the SNR needed for the target BER and the estimated SNR in dB.

$$b_n = \log_2\left(1 + |g_n|^2 \frac{\text{SNR}[n]}{\Gamma_n \lambda_n}\right) \tag{1.16}$$

$$\lambda_n = \text{SNR}[n] - r\text{SNR}(b_n) \tag{1.17}$$

Bit allocation is performed by starting with $b_n = 0 \forall n$. The projected margin $\mathcal{M}_n$, the

SNR margin for b_n+1 bits, is then computed for all subcarriers. b_n is increased by one bit for the subcarrier with the largest margin and $\mathcal{M}_n$ is updated. This repeats until $\max(\mathcal{M}_n) \leq 0$.

$$\mathcal{M}_n = \mathrm{SNR}[n] - r\mathrm{SNR}(b_n + 1) \tag{1.18}$$

As the receiver must know the number of bits assigned to each subcarrier in order to demodulate the data packet, the information must be sent to the receiver prior to transmitting data. Alternatively algorithms to detect the modulation order can be employed with some additional complexity [12].

1.1.3.2 Adaptive Power Loading

Following adaptive bit loading, the SNR margin λ_n will be non-uniform across the subcarriers. This is due to the need for a discrete number of bits to be assigned which means that $r\mathrm{SNR}(b_n)$ will also be discrete while SNR is not. The result of non-uniform λ_n is that the estimated BER will be different across subcarriers. By allocating different amount of power to different subcarriers, the subcarriers can be equalized.

First the sum of all SNR margins for all subcarriers is computed to get the geometric margin γ. Then the unnormalized gain $\mathfrak{g}_n$ in a linear scale is calculated. Subcarriers where the estimated SNR was too low to transmit any bits are given $\mathfrak{g}_n = 0$ as their power is reallocated to other subcarriers.

$$\gamma = \sum_{\substack{n=0 \\ b_n>0}}^{N-1} \lambda_n \tag{1.19}$$

$$\mathfrak{g}_n = \begin{cases} 10^{(\gamma-\lambda_n)/10} & b_n > 0 \\ 0 & b_n = 0 \end{cases} \tag{1.20}$$

The gain g_n is then calculated by reconverting $\mathfrak{g}_n$ into a dB scale and normalizing it.

$$g_n = \mathfrak{g}_n \sqrt{\frac{1}{\sum_{n=0}^{N-1} |g_n|^2}} \tag{1.21}$$

The gain is applied to the data packet prior to the IFFT. At the receiver the gain is removed before the QAM data is demodulated.

1.2 Experimental Setup

The setup involves three layers as can be seen in Figure 1.2. In the computational layer, waveforms are generated and analyzed using a custom Matlab code base. The waveforms are uploaded to the AWG where they are converted into analog signals. The transmitter (Tx) module converts the electrical signals to optical signals which are then transmitted via an emissive optical fiber. Collection optics direct light into the receiver (Rx) which converts from optical signals to electrical signals. The RTO performs analog to digital conversion on the received waveforms which are then read by Matlab and analyzed.

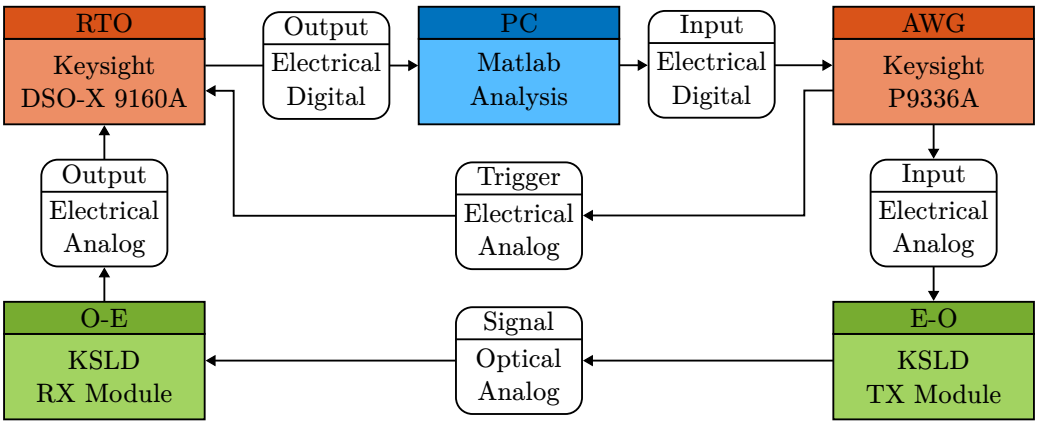

Figure 1.2: Experimental setup schematic. The computational layer (blue), the digital-analog conversion layer (orange), and the transceiver layer (green).

The optical path consists of an emissive fiber affixed to a parabolic reflector intended to mimic a segment of the optical rotary interface as seen in Figure. 1.3. The reflector is translated along the fiber's length to derive longitudinal measurements. Alternatively, the distance between the reflector and the detector is changed to derive radial distance measurements. A detailed description of the optical system is reserved for Chapter. 3.

AWG Settings	
Sample Rate	1.28 GSa/s
Vertical Resolution	16-bit
Analog Bandwidth	540 MHz
Single Channel V_{pp}	0.5 V

RTO Settings	
Sample Rate	2.5 GSa/s
Vertical Resolution	12-bit
Analog Bandwidth	450 MHz
Single Channel V_{pp}	1 V

Table 1.1: Analog-digital conversion equipment specifications.

Min Frequency	Max Frequency	Clipping Factor	Guard Interval	Pilots	BER Target
0.25 MHz	350 MHz	3σ	0.2%	128	3×10^{-3}

Table 1.2: OFDM symbol parameters.

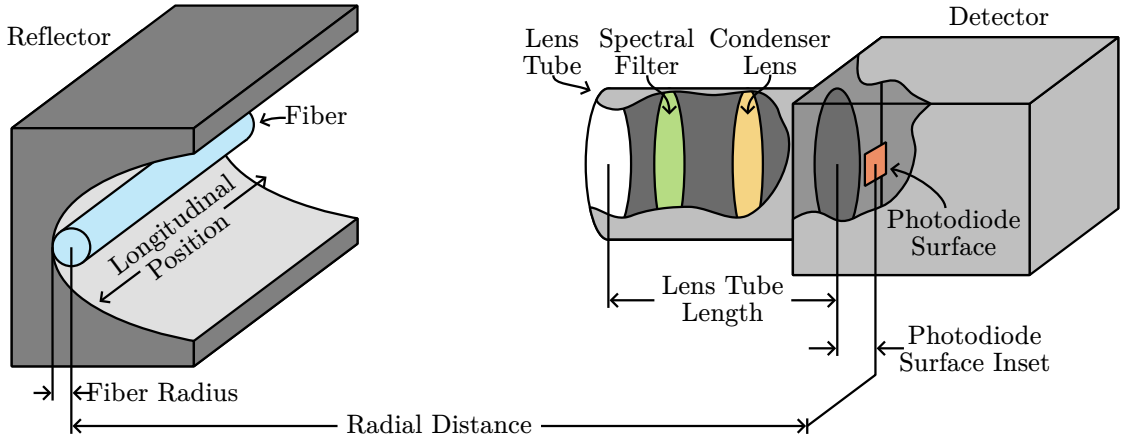

Figure 1.3: Experimental setup diagram. The fiber cross-section is shown as the fiber is 2 m long and connected to the KSLD TX Module at both ends.

Transmitter	
Wavelength	850 nm
Optical Power	62 mW
Modulation Type	Direct

Detector	
Photodiode Diameter	1.5 mm
Wavelength Range	400 nm to 1000 nm
Bandwidth	20 kHz - 470 MHz

Table 1.3: Electrical-optical conversion specifications.

Emissive Fiber	
Fiber Length	2 m
Fiber Radius	1 mm
Fiber Attenuation	3.7 dBm/m

Collection Optics	
Lens Diameter	25.4 mm
Spectral Filter λ_0	850 nm
Lens Tube Length	26.2 mm

Table 1.4: Optical equipment specifications.

Results and Discussion

2.1 Adaptive Bit and Power Loading

In order to implement adaptive bit and power loading, accurate SNR requirements for the different constellations are required. The theoretical relationship was verified to ensure that a consistent SNR definition is maintained.

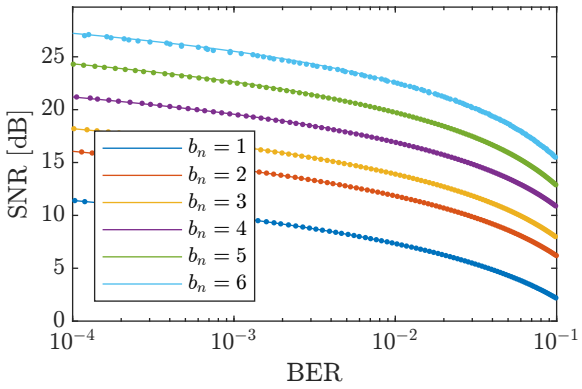

Figure 2.1: Simulated SNR as a function of BER.

In Figure. 2.1, the relationship between SNR and BER is simulated. White Gaussian noise of varying amplitude is added to QAM data of different orders before it is demodulated and its BER measured. The relationship is then inverted and a rational polynomial fit of degree 2 is applied. This method is used for simplicity as the signal power parameter for the white Gaussian noise function, `awgn`, is consistent with the SNR calculated using Matlab's modulation error ration function, `comm.MER`, which is equivalent to SNR in this application. Data from 5,000 OFDM symbols is used to generate the SNR map shown in Figure. 2.2a, which is used to generate experimental results.

Using the BER vs SNR curves, the SNR vs frequency data, and the algorithms described in Section. 1.1.3.1, bit and power maps can be determined for the subcarriers. In Figure. 2.2a, the measured SNR and the required SNR, rSNR, of the experimental system are

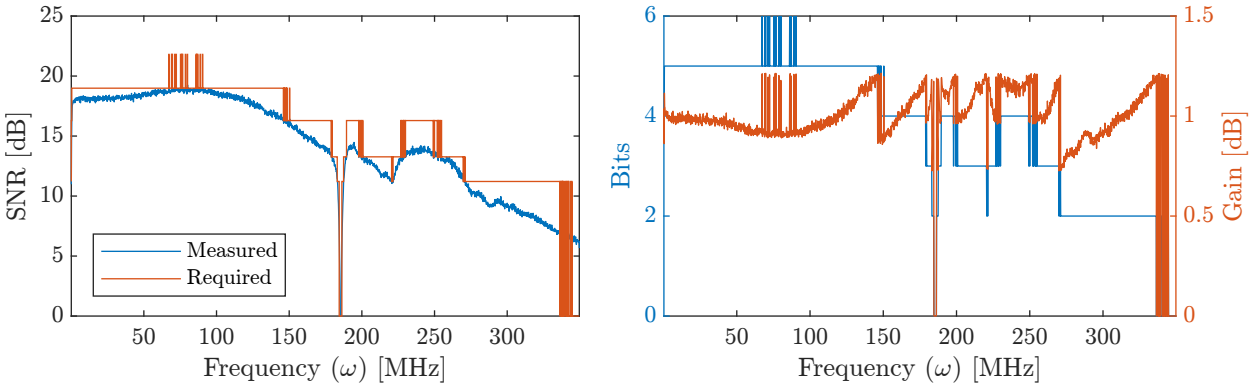

(a) SNR map

(b) Bit and power maps

Figure 2.2: Adaptive bit and power loading maps.

plotted. Using this data, the number of bits and gain for each subcarrier are plotted in Figure. 2.2b. The number of bits per subcarrier is equivalent to the QAM modulation order, 2 bits indicating 4-QAM, 3 bits indicating 8-QAM, and so forth. The power from subcarriers with gain less than 1 is allocated to the subcarriers with gain greater than 1.

2.2 Channel Correction

Training symbol assisted and pilot assisted channel estimation and compensation are used to optimize the performance of the system. The training symbol assisted channel estimation is intended to compensate for general long term channel effects while the pilot assisted channel estimation is used to compensate for short term effects.

2.2.1 Training Symbol Assisted

To estimate the channel, 5,000 OFDM symbols are used to perform a training symbol assisted channel estimation. The same training symbols are used to measure the SNR vs frequency relation of the system used for adaptive bit and power loading. The number of training symbols thus determines the quality of the adaptive bit and power loading schemes and channel correction. However, a training symbol takes the place of a data symbol and therefore reduces the throughput of system. In an operational system, the number of training symbols must be optimized to the variability of the channel. As the experiments are performed on

a static system and the characteristics of the dynamic channel are unknown, the training symbols are transmitted and processed prior to data transmission and are not included in the overhead of the data rate measurements.

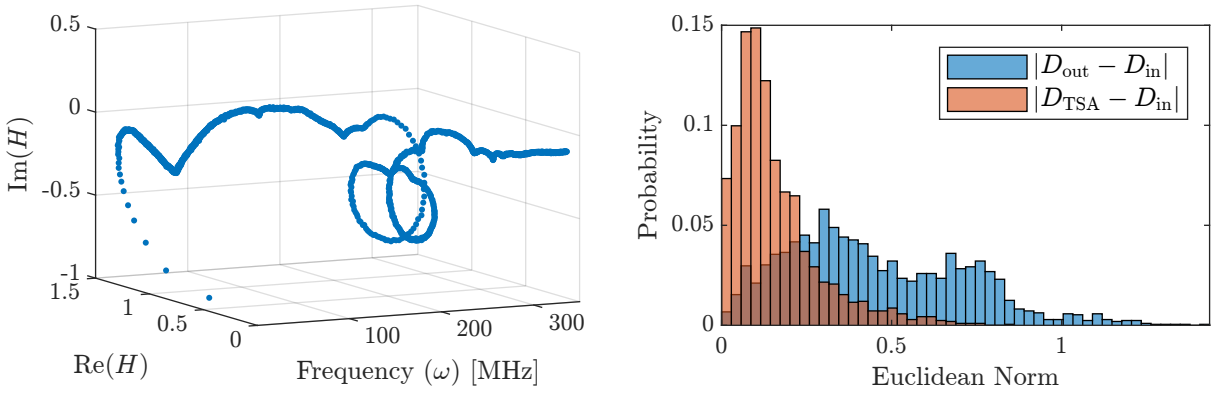

(a) Transfer Function (b) Histogram

Figure 2.3: Training symbol assisted channel estimation.

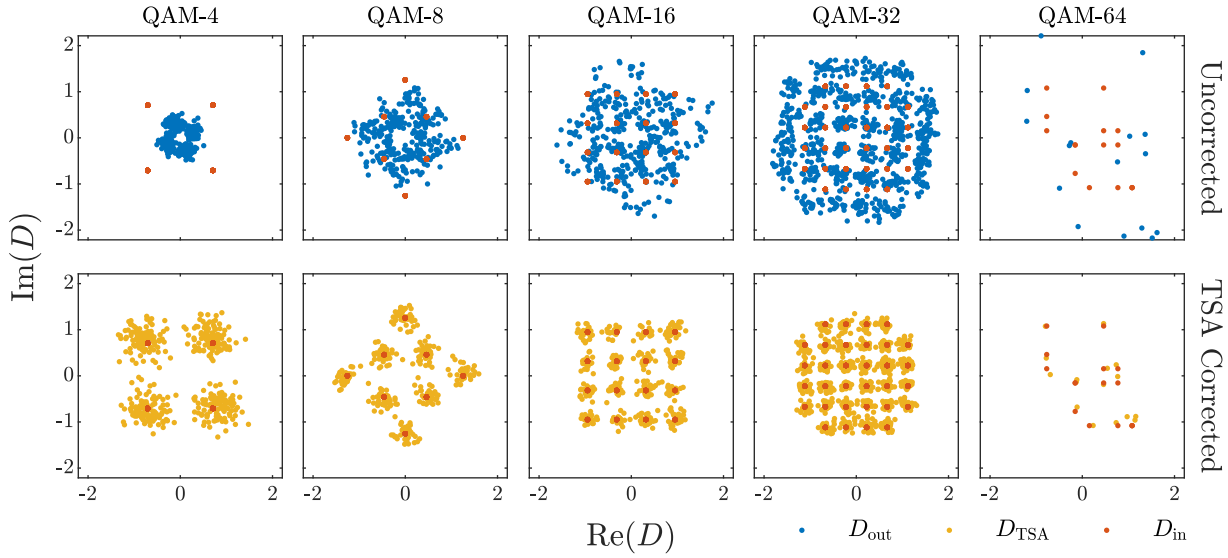

Figure 2.4: Sample comparison of training symbol assisted channel correction.

In Figure. 2.3a, the transfer function is plotted for all subcarriers. In Figure. 2.3b, a histogram of the euclidean distance between the uncorrected output data D_{out} and input data D_{in}, and the training symbol assisted corrected data D_{TSA} and D_{in} is shown. The mean distance from D_{in} for D_{out} is 0.453 ± 0.261, and for D_{TSA} is 0.157 ± 0.127.

2.2.2 Pilot Assisted

Pilot assisted channel estimation and compensation is performed on the received output data after the training symbol assisted estimation and compensation is performed. A sample two-step pilot assisted channel estimation and compensation is shown on output data has not been otherwise corrected to demonstrate the CPE and CFO corrections steps.

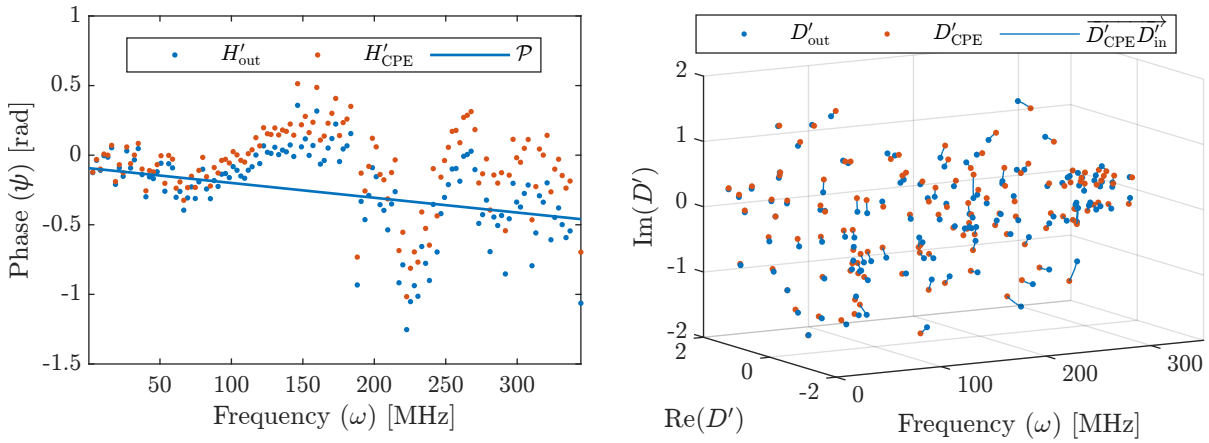

(a) Phase (b) 3D Constellation

Figure 2.5: Sample pilot CPE correction.

In Figure. 2.5, a sample pilot assisted CPE correction is shown. 128 out of 2085 occupied subcarriers are used as pilots and a fitted phase slope of $\phi = -1.06 \times 10^{-3}$ rad/MHz is found. Figure. 2.5a shows the pilot phase versus frequency before and after CPE correction and Figure. 2.5b shows the effect of CPE correction on the subcarrier data.

Figure. 2.6 shows a sample pilot assisted CFO correction. The 128 CPE corrected pilots from Figure. 2.5 are used. In Figure. 2.6a, transfer functions are plotted as a function of subcarrier frequency. A polynomial fit of degree 11 is used to fit to H'_{CPE}. In Figure. 2.6b the effect of CFO correction on the pilot subcarrier data is shown.

In Figure. 2.7 a sample of the pilot data evolution is shown as it undergoes a two-step pilot assisted channel estimation and compensation. The 128 CPE and CFO compensated pilots from Figure. 2.5 and Figure. 2.6 are used. Lines are used to show the distance between the pilot data at each step and its corresponding pilot input data. The Euclidean distance

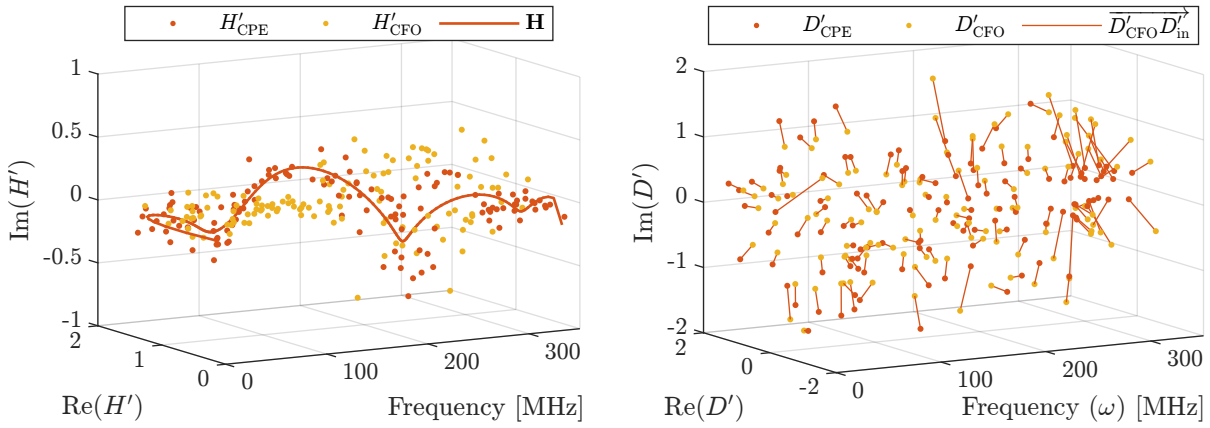

(a) Transfer function (b) 3D Constellation

Figure 2.6: Sample pilot CFO correction.

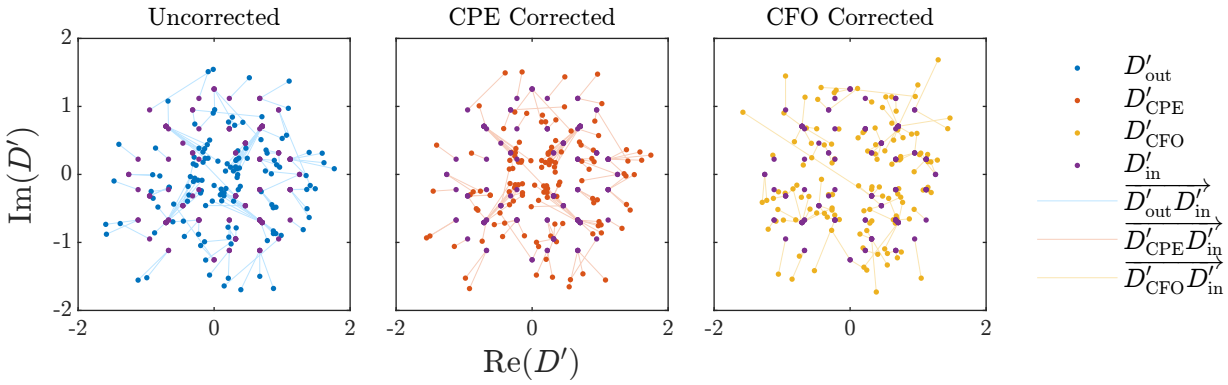

Figure 2.7: Sample pilot correction constellation diagrams.

from the input data is used as an error metric as it will contribute to the QAM demodulation performance and final BER.

The Euclidean distance between the data at each step and the input data for all subcarriers is visualized in Figure. 2.8. The channel compensation is extrapolated from the pilots through interpolation of the CPE and CFO fits. In Figure. 2.8a, a general improvement at each step is seen with exemptions occurring at the lowest frequencies and near 190 MHz. These are examples of interpolation errors which will degrade the performance of certain subcarriers. In Figure. 2.8b, a histogram of the data in Figure. 2.8a is shown and the improvement at each step is quantified. The uncorrected data is found to have a mean Euclidean distance of 0.453 ± 0.261, 0.421 ± 0.227 for the CPE corrected data, and

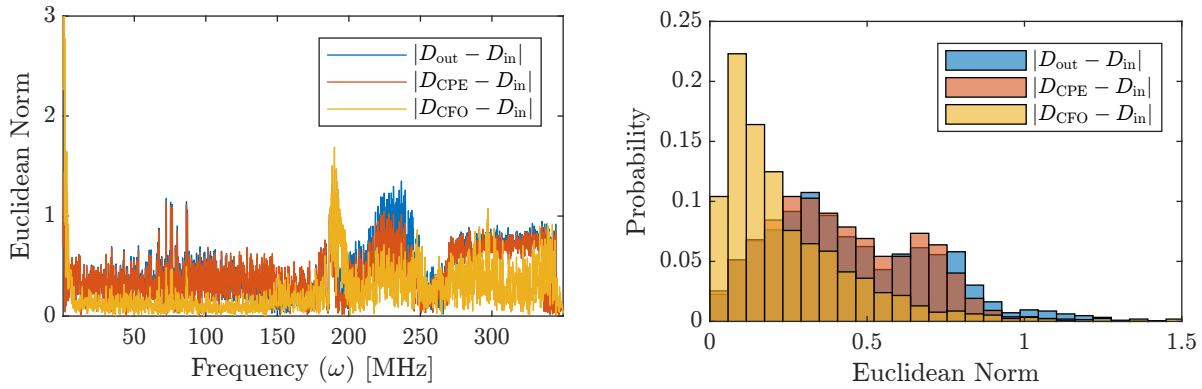

(a) Euclidean Norm (b) Histogram

Figure 2.8: The effect of pilot assisted channel estimation on the Euclidean distance to the input data.

0.265 ± 0.349 for the CFO corrected data. Thus, despite the interpolation errors, the pilot assisted correction is effective at improving the system performance for the demonstrated OFDM symbol. A higher number of pilots reduces the amount of interpolation error but reduces the data capacity of the symbol. The optimal number of pilots needed depends on the channel quality and the subcarrier spacing.

When the training symbol assisted channel correction is performed prior to pilot assisted channel correction, a polynomial of degree 3 is used for the CFO fit as the majority of the channel effects are already compensated for and a higher polynomial fit will result in over-fitting. Across all 5,000 OFDM symbols, when the pilot assisted channel compensation was performed after training symbol assisted compensation, it resulted in a reduction of the Euclidean distance of 22.0%, from 0.188 ± 0.141 to 0.147 ± 0.112. The CPE compensation was found to reduce the distance by 21.0% with a further reduction of 1.3% from the CFO compensation.

The CPE compensation is seen to contribute more than the CFO compensation when pilots are used in combination with training symbols. In a static application, removing the CFO correction and reducing the number of pilots may increase data rates for an equivalent BER. As the intended application is dynamic, the training symbol assisted channel estimated is expected to be less effective and the symbol to symbol variation is expected to increase.

In these conditions, the CFO correction is expected to be of greater benefit and is thus kept.

2.3 Performance

The performance of the system is measured in two ways; at two positions along the length of the fiber at a fixed radial distance, and at a fixed position along the length of the fiber at three radial distances from the fiber.

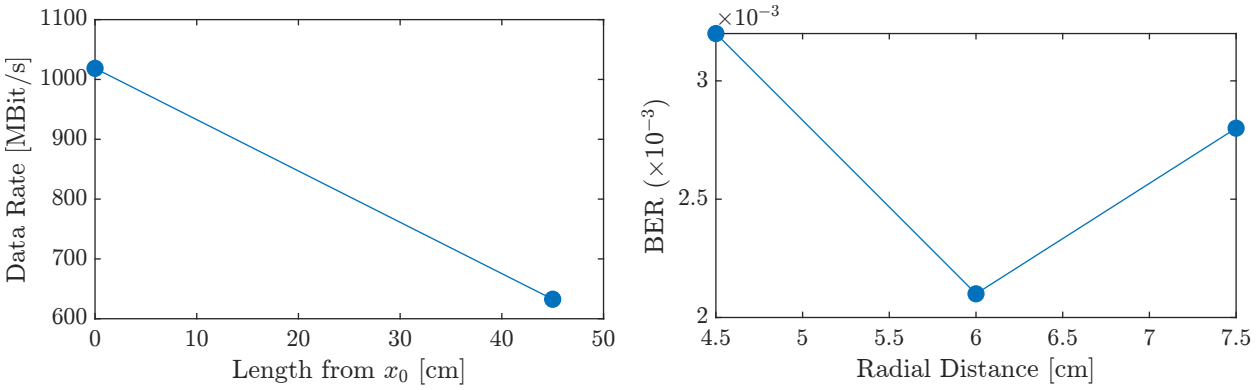

(a) Data rate versus longitudinal position

(b) BER versus radial distance

Figure 2.9: System performance using adaptive bit and power loading with training symbol assisted and pilot assisted channel estimation and compensation.

In Figure. 2.9a, the data rate at a fixed BER of 1×10^{-3} is measured at two longitudinal positions along the fiber length. The positions are taken relative to the lengthwise center of the emissive fiber. The detector is placed at the minimum distance to the fiber which results in 4.5 cm between the radial center of the fiber and the detector's photodiode. A new channel estimation and SNR map are produced for each position. The greater performance margin seen at 4.5 cm is assumed to be due to a less extensive channel estimation at 4.5 cm than the one performed at 0 cm.

In Figure. 2.9b, the detector is placed at the central point along the length of the fiber and at the minimum radial distance from the fiber, 4.5 cm, a channel estimation and SNR map are produced and the BER is measured. The data rate is 1018.6 Mbit/s. The detector is then moved to a radial distance of 6.0 cm and 7.5 cm without updating the channel estimation or SNR map. As such the data rate for the given BER target is the same at each position

and the BER is thus measured.

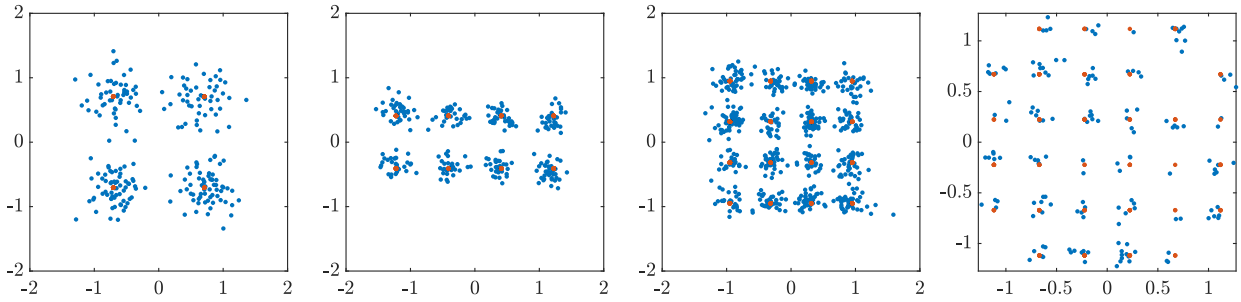

(a) QAM 4 (b) QAM 8 (c) QAM 16 (d) QAM 32

Figure 2.10: Sample constellation diagram. Red, transmitted data, blue, received data.

A sample constellation diagram is shown in Figure 2.10. The sample is taken at the middle of the fiber with the minimal distance of 4.5 cm between the fiber and the photodiode. The BER achieved is 2.7×10^{-3} with a data rate of 1018.6 Mbit/s. The different QAM orders are plotted separately for visibility. It is evident from the clustering of subcarriers in Figure. 2.10 that the adaptive bit and power loading algorithm is successfully classifying the subcarriers based on their SNR.

Part II

Simulation Architecture

Methods

Three components are utilized to in the experimental methodology, experimental measurements, analytical models, and simulation models. The analytical model is fitted to the experimental measurements to help determine values for the simulation model. Data from the simulation model is then compared with the experimental measurements to determine the accuracy of the simulation architecture. The simulation models can then be used to characterize the optical system with standalone results.

Although there is a unified goal, the individual experimental measurements are varied enough that the unique characteristics of their experimental measurements, analytical models, and simulation models have been moved to their respective results sections for the ease of the reader. Information common to multiple measurements is found below.

3.1 Experimental Components

To verify the results from the simulations, physical experimental measurement setups are constructed. These experimental measurement setups are what the simulations are modeled after.

3.1.1 Optical Source

Two optical sources are used, a baseline red laser and the KSLD Tx module. The KSLD source is capable of outputting at two wavelengths, a 850 nm IR output and a 450 nm white output. The 450 nm output is generated from a phosphor layer which makes it a broadband white light source. All three sources are fiber coupled however the connector types are different across the two devices.

The spectrum of the KSLD IR optical source is given in Figure. 3.1. The Gaussian fit provides a central wavelength (CWL) of 849.7 nm and a full-width half-maximum (FWHM)

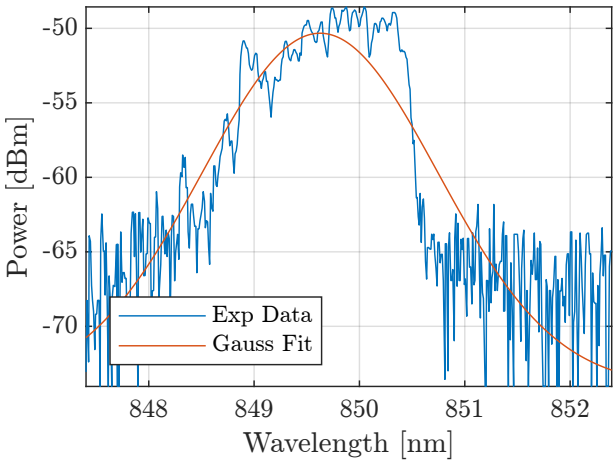

Figure 3.1: KSLD Tx Module IR spectrum.

Table 3.1: Optical source specifications.

Source	Wavelength	Power	Connector
Baseline Red	635 nm	0.5 mW	FC/APC
KSLD IR	850 nm	62 mW	Fakra
KSLD White	450 nm	250 mW	Fakra

of 2.09 nm. The optical spectrum analyzer used had a lower limit of 800 nm thus the KSLD white light source and baseline red optical source could not be measured.

3.1.2 Fiber Connectors

The fiber-optic connector/angled physical contact (FC/APC) and KSLD FAKRA fiber connectors are shown in Figure. 3.2.

The FC/APC connector is used with the baseline red optical source and Versalume fiber. The KSLD FAKRA connector is used with the KSLD IR and white optical sources and KSLD emissive fiber.

The FAKRA connector is a modified version of the Molex FAKRA connector. The RF connector is replaced with a fiber ferule to produce a fiber connector with enhanced environmental resistance.

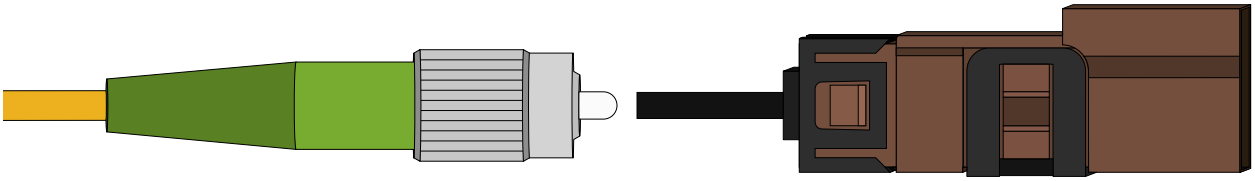

(a) FC/APC (b) FAKRA

Figure 3.2: Fiber connectors

3.1.3 Emissive Fibers

A connectorized Versalume fiber with a 1 m diffusion length is used. This translates to an attenuation coefficient of 10 dBm/m. The fiber diameter is 0.9 mm.

The KSLD fiber is measured to have a length of 2 m and a diameter of 2 mm. The diffusion length of the KSLD fiber is unkown.

The Versalume fiber has a silica core with submicron scattering centers for wavelength independent scattering. The magnitude of scattering is controled via the size of the scattering centers [13]. The mechanism of scattering for the KSLD fiber is unknown but assumed to be similar.

3.1.4 Parabolic Reflector

The approximate physical dimensions of the parabolic reflector provided by KSLD are shown in Figure. 3.3. It is 3D printed with the parabolic section covered in aluminum foil type material.

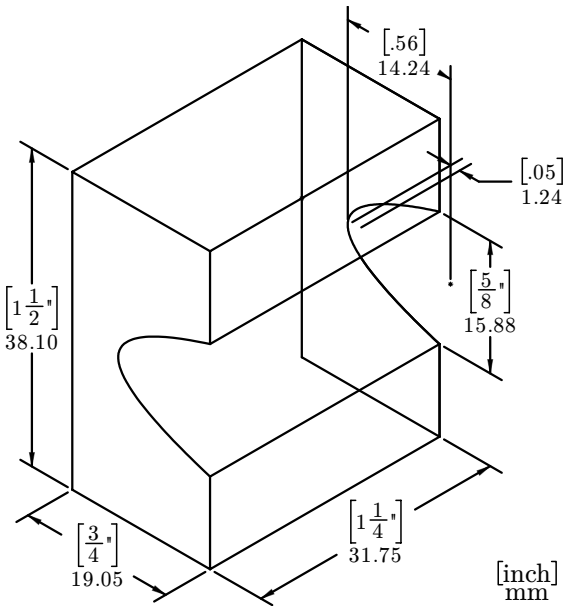

Figure 3.3: Approximate physical dimensions of the parabolic reflector.

3.1.5 Lens and Filter

The lenses and filters provided by KSLD are thought to be aspheric condenser lenses and spectral filters from Thorlabs. Their item numbers are assumed based off of their diameters and operating wavelengths. The lens and filter are packaged together in a 26.2 mm long lens tube and could not be uncoupled for individual testing.

Table 3.2: Condenser Lenses

Setup	Item #	Coating
White	ACL25416U-A	350 to 700 nm
IR	ACL25416U-B	650 to 1050 nm

Table 3.3: Spectral Filters

Setup	Item #	CWL	FWHM
White	FB450-40	450 ± 8nm	40 ± 8nm
IR	FB850-40	850 ± 8nm	40 ± 8nm

3.1.6 Power Meter and Detector

The power meter used for all the experimental measurement is the Newport 2832C. The power meter is used with the 818-ST/CM wand style detector.

The detector has a power range of -70 to 33 dBm (0.1 nW to 2 W) and a detection area of 1 cm $\times$ 1 cm. The applicable wavelength range is 400 to 1100 nm and it has an accuracy of $\pm 2\%$.

To reduce the measurement error, the power meter is set to sample at 25 Hz and 50 samples for each data point are recorded. The mean and standard deviation of the 50 samples is used to fit to the analytical models. The detector is zeroed before each set of measurements to remove the background power. The detector is used in conjunction with its calibration module and the power meter is set to the relevant wavelength for accurate measurements.

3.2 Simulation Environment

The simulation environment is developed in Zemax OpticStudio which uses ray tracing to simulate optical systems. Ray tracing is the technique by which light is assumed to take the form of rays. The path these rays take through an optical system is then computed.

3.2.1 Sequential vs Non-Sequential

There are two methods of ray tracing that Zemax OpticStudio implements, sequential ray tracing (SRT) and non-sequential ray tracing (NSRT). In sequential ray tracing, the components of an optical system can effectively be translated into matrix transforms. The system is then represented by the product of these matrices. The resulting matrix can then be solved to determine information about the system such as effective focal length, magnification, and spot size. The limitation of this method is that the optical path is determined sequentially. The order in which the components' matrices are combined changes the resulting system matrix. Thus, if there are multiple paths through an optical system, each path would need to be represented by its own system matrix.

Non-sequential ray tracing systems are similar in that the components can be represented by matrix transforms but differ in that the component's matrices are not combined and no system matrix is found or solved. Instead, a number of rays are simulated and the path through the optical system is calculated for each ray. This method is more akin to how lighting is simulated in a video game or 3D environment.

A ray is created with an initial position and direction, the first intersection with an object in its path is determined and the new ray position and direction is calculated based on the ray's interaction with the object.

This process is repeated for a multitude of rays which form a representative sample of the light going through the system. Additionally, each ray represent a fractional amount of power to simulate the flow of power through the system.

The drawback to NSRT is that it is much more computationally intensive compared to SRT. Aside from needing to calculate ray interceptions for each step for each ray, calculating the system matrix once then applying it to all rays or using it to solve for parameters is much more efficient than applying the same transforms to each ray separately.

The reason why NSRT is still used despite these drawbacks is that it is capable of simulating systems that could not be simulated by SRT. One example that will be explored in

Section. 3.2.2, is NSRT's application to non-imaging systems.

3.2.2 Non-Imaging Systems

A major advantage of NSRT over SRT is the ability for NSRT to simulate non-imaging systems. Non-imaging systems are systems where no image of the source is produced. Instead in non-imaging systems, the flow of power through the system is the main concern. In such systems, the source may be diffuse, the optical path may not be consistent across rays, and non-idealized geometry may be important.

A diffuse optical source is a source which extends over a large area and where initial ray directions are more-or-less random. This makes the source difficult to image but more importantly it often results in multiple different paths through an optical system. As an example, consider some rays bouncing off an adjacent surface prior to being reflected into a lens. This would require two system matrices in an SRT system, one for the light which goes directly into the lens, and another for the light which isn't directly incident on thelens. If we also take into account multiple prior surface reflections, or reflection from a non-idealized lens, the number of potential system matrices becomes unmanageable and the amount of light to assign to each becomes difficult to determine.

Even with a traditional idealized optical source, non-idealized optical components, e.g., components which have a non-zero reflectance, can similarly result in multiple optical paths through a system.

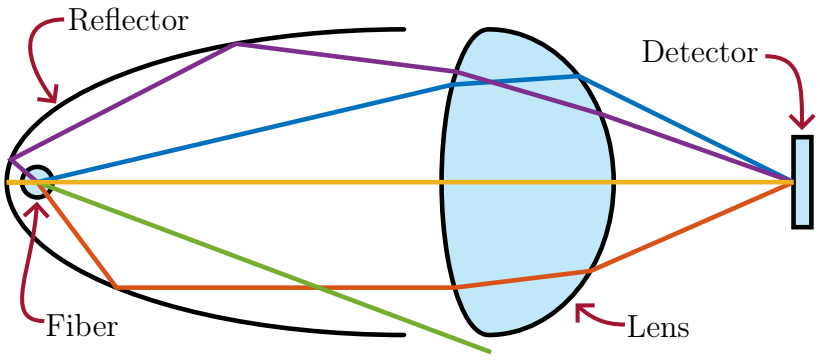

Figure 3.4: Potential paths through an optical system.

The optical system for which we are developing a simulation architecture is a non-imaging system where the flow of power through the system is the primary concern. An emissive fiber is a diffuse source which will produce rays in all directions at random. In addition, the optical system may implement components such as a parabolic reflector. This means that at a minimum there are two optical paths through the system, one where light goes from the fiber directly to the lens, and another where the light goes from the fiber to the parabolic reflector then to the lens. For completeness, there are edge cases such as when the light may go from the fiber to the parabolic reflector then back to the fiber, or where there are multiple reflections off of the parabolic reflector before the ray is incident on the lens.

3.2.3 Glue Distance

Glue distance is the minimum distance between two objects before which the two objects are considered touching. Having an interface between two objects can greatly alter an optical system. Ensuring that objects which should be touching are below this distance and object which shouldn't be touching are above this distance ensures that the intended optical system is simulated.

3.2.4 Polygon Quality

The geometric bounding regions of simulated objects is determined via an iterative process to find exact ray intercepts. However, the drawing resolution is first used to determine if a ray is close enough to an object to begin the iterative process. For this reason, when objects are large or have complex shapes, having a drawing resolution that is too low may result is errors.

The drawing resolution does not need to be set needlessly high as it will impact the ray tracing performance. As long as the resolution is high enough that it can be used as an estimate of the objects bounding box, greater resolution will not increase the simulation accuracy.

3.2.5 Scattering

The emissive fiber is assumed to have Lambertian scattering characteristics which are simulated using scattering, ray splitting, and thin window scattering.

Scattering is simulated via scattering algorithms which define the likelihood of a rays final direction given its incident direction. The final ray direction is directly connected to the energy distribution of the physical scattering system. If x percent of the energy goes in direction $\vec{a}$ in the physical model, then in the simulation the ray will be scattered in direction $\vec{a}$, x percent of the time.

Ray splitting must be enabled in Zemax in order to enable scattering. Ray splitting is the mechanism by which an incident ray will be split into multiple final rays upon scattering. This enables the portion of the energy which is scattered to be tuned and could give a better approximation of the scattering effect in the simulations. The final rays still follow the scattering probability rules previously defined but by increasing the number of final rays the scattering effect can be better approximated if only a few rays are scattered. In this system, the number of final rays is set to 1 as all rays will be scattered.

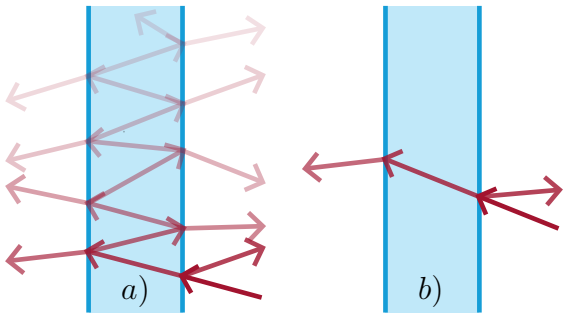

Figure 3.5: Example of ray paths inside a volume with a) regular scattering, and b) thin window scattering.

Thin window scattering is a feature that limits scattering to speed up the simulation in places where more rigorous scattering is not needed. Thin window scattering is used when internal reflections inside an interface are unimportant to the results of a simulation. A portion of light can get trapped between two optical interfaces due to the scattered reflection

when exiting a material, see Figure. 3.5. Each subsequent internal reflection may produce more reflections until the minimum ray power limit is reached and the ray is terminated. Dealing with an optical interface in this manner is computationally expensive and when the portion of light trapped is small or otherwise irrelevant it is better to simply disregard the internal reflections. Thin window scattering limits scattering to the initial reflection and the final transmitted ray, removing internal reflections. The same portion of light will be reflected and transmitted by the object as with regular scattering but results can differ depending on the importance of internal scattering.

In the optical rotary interface simulation model, thin window scattering is used on the emissive fiber model. In a complete fiber model, internal scattering would be an important mechanism for the fiber. However, given that the rays are produced randomly by the source filament object, the diffusive characteristic of internal scattering is recreated to an acceptable degree. Additionally, as the coupling between the optical source and the emissive fiber is unknown, the only metric of relevance is the amount of emitted light by the fiber. Simulating the fiber with internal reflections would require that the power of the light injected into the fiber is tuned. Instead, with the source filament, the power per unit length of the fiber can be set which is closer to measurable quantities. As a result, because the difference between a model of the fiber with internal reflections or with a source filament and thin window scattering is small, and the computational requirements of the first option are so much higher, the latter model is used.

3.2.6 Simulation Components

The simulation environments utilize a number of common components across the various configurations. The implementation of these common components is described below.

3.2.6.1 Detectors

The simulated detectors are given the dimensions of the experimental detector described in Section. 3.1.6. As the experimental detector has a single detection area, the simulated

detector is described by a one pixel by one pixel detector and set to record incoherent irradiance data. Zemax's default values are used for the remaining detector parameters.

3.2.6.2 Emissive Fiber

As the construction of the tested physical fibers is not known, the fiber material is not assumed but is instead simulated as a diffuse source. The emissive fiber is simulated using a source filament and a cylinder volume. The source filament is placed at the radial center of the cylinder volume and the length set such that the source filament is 0.1 mm shorter than the cylinder volume for reasons described in Section. 3.2.3. The emission length of the fiber is thus 0.2 mm less than the length of the simulated fiber.

The cylinder volume is set to have the physical dimensions of the simulated fiber. To simulate the fiber as a diffuse source, the cylinder surface is set to posses a Lambertian scatter model, with a scatter fraction of 100%. As described in Section. 3.2.5, to avoid unnecessary computation, the cylinder volume is set to use thin window scattering.

3.3 Analytical Models

An analytical model is used to determine parameters of interest from theexperimental measurement. These parameters can then be input into associated simulations as a means of translation between physical and simulated systems. Radiometry is used to construct the analytical models. Radiometry is a geometric approach for measuring electromagnetic radiation.

The primary relevant radiometric quantity is irradiance, which is defined as the radiant power received by a surface per unit area. Radiant power is measured in Watts and irradiance is given in Watts/meter^2. The term detected power thus is more explicitly give as the detected radiant power. Similarly, source power is more accurately described as radiant exitance, which is the radiant power emitted by a surface per unit area.

Measurement Setups

4.1 Calibration

To determine the optical power of the sources and to calibrate the measurement apparatus, the power from the fiber connectors is measured. A detector is placed in the beam path at varying distances from the connector to observe the expected inverse-square law relationship between irradiance and distance to a point source.

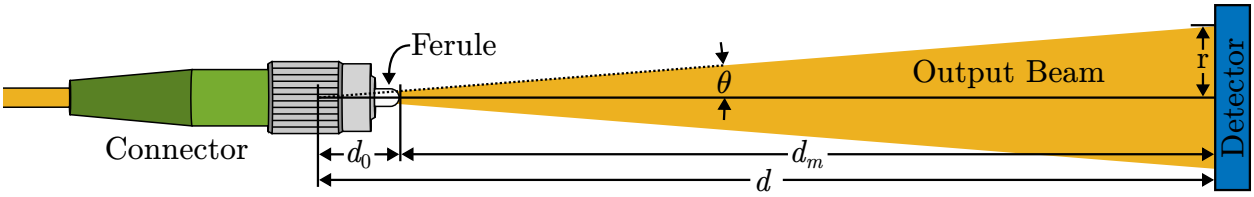

Figure 4.1: Measurement schematic for source power testing.

Figure. 4.1, details the setup and relevant parameters. The primary setup components include the fiber connector, the output beam, and the detector surface.

4.1.1 Experimental Setup

The fiber connectors are mounted in a fixed position. The detector is placed on a translation stage and aligned with the beam from the connector. The power is read from the detector using an automated script at a series of distanced from the connector.

Two setup configurations are used; the baseline red laser with the FC/APC connector, and the KSLD IR module at 850 nm with the modified FAKRA connector. The power meter attenuator is used at short distances with the KSLD IR source to not overload the detector.

4.1.2 Analytical Model

A geometric analytical model is used to approximate the physical system so that it is analogous to the ray tracing based simulation model. The geometric analytical model assumes

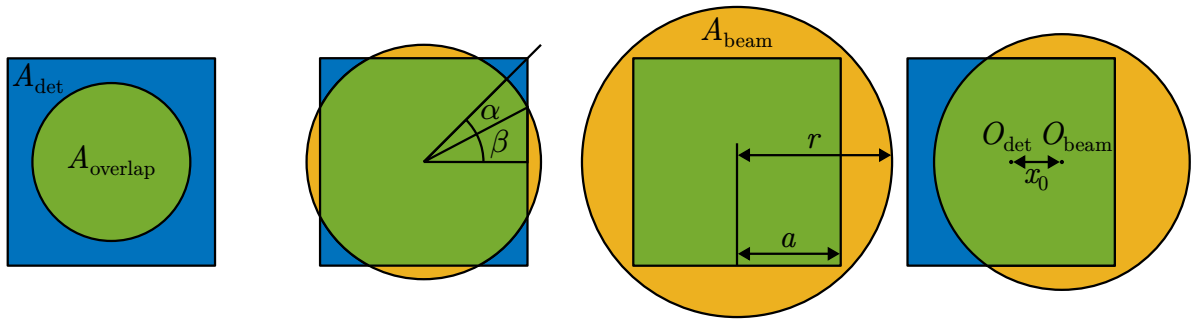

(a) $r \leq a$ (b) $a < r < a\sqrt{2}$ (c) $a\sqrt{2} \leq r$ (d) Origin offset

Figure 4.2: Beam overlap parameters

that the beam is conic, of uniform intensity across the beam front, originating from a point source, and that the beam and detector are aligned normally and centrally. As the beam radius at the end of the fiber ferule is not infinitely small, an offset distance is added to the model. Thus, the measured distance from the end of the fiber ferule to the detector surface, d_m, plus the distance offset, d_0, is equal to the true distance, d, as seen in Figure. 4.1.

The beam radius at the detector, r, is determined from the beam divergence, θ, and the distance, d.

$$r = d\cos^{-1}(\theta) \tag{4.1}$$

$$= (d_m + d_0)\tan^{-1}(\theta) \tag{4.2}$$

4.1.2.1 Beam-Detector Overlap

To construct an analytical model, the percentage of the beam area that is incident on the detector is assumed to be equal to the percentage of the beam's power that is incident on the detector. Thus, to determine a relationship between measured power and distance, the beam-detector overlap area must be computed.

In Figure. 4.2 the overlap domains and parameters are shown. The detector area, A_{det}, is shown in blue. The beam area, A_{beam}, is shown in yellow. The region where A_{det} and A_{beam} overlap is the overlap area, A_{overlap}, and is shown in green. α is the wedge angle in radians, β is the triangle angle in radians, a is the detector half-width, and r is the beam radius.

In Figure. 4.2.a, the entire beam area is encompassed by the detector area. The detected power is therefore equal to the beam power. Conversely, in Figure. 4.2.c, the entire detector area is encompassed by the beam area. The detected power is then proportional to the ratio of overlap area to beam area, where overlap area is equal to detector area. In Figure. 4.2.b, neither the detector or beam areas encompass the other. The detected power is the ratio of overlap area to beam area, however, the overlap area must be computed as the sum of circular and triangular sections. In Figure. 4.2.d, the distance offset, x_0, between the detector origin, O_{det}, and the beam origin, O_{beam}, is shown.

$$P_{\text{det}} = \begin{cases} P_{\text{beam}} & \text{if } r \leq a \\ P_{\text{beam}} \frac{A_{\text{overlap}}}{A_{\text{beam}}} & \text{if } a < r < a\sqrt{2} \\ P_{\text{beam}} \frac{A_{\text{det}}}{A_{\text{beam}}} & \text{if } a\sqrt{2} \leq r \end{cases} \tag{4.3}$$

In Figure. 4.2.c, the overlap area are computed by splitting the area into circular sectors and right angle triangles. The sectors have area A_s, angle α, and side length r. The right angle triangles have area A_t, angle α, and side lengths a and r.

If $O_{\text{det}} = O_{\text{beam}}$, then the overlap area can be split about the center into eight equal parts. Each part being $\pi/4$ radians and having one sector and one triangle. It follows then that,

$$\alpha = \pi/4 - \beta \tag{4.4}$$

$$\beta = \cos^{-1}(a/r) \tag{4.5}$$

α and β are used to find A_s and A_t using the equations for the area of a sector and the

area of a triangle respectively.

$$A_s = \frac{\alpha r^2}{2} \tag{4.6}$$

$$A_t = \frac{ar\sin(\beta)}{2} \tag{4.7}$$

Relationships for A_{overlap}, A_{det}, and A_{beam} in terms of a and r follow.

$$A_{\text{overlap}} = 8(A_s + A_t) \tag{4.8}$$

$$= 8\left(\frac{\alpha r^2}{2} + \frac{ar\sin(\beta)}{2}\right) \tag{4.9}$$

$$= (\pi - 4\beta)r^2 + 4ar\sin(\beta) \tag{4.10}$$

$$A_{\text{det}} = (2a)^2 \tag{4.11}$$

$$A_{\text{beam}} = \pi r^2 \tag{4.12}$$

4.1.2.2 Fit Parameters

The analytical model is fitted to P_{det}. To determine the fit parameters, the relations for dependent quantities are traced back to common variables, starting from Equation. 4.3,

$$P_{\text{det}}(P_{\text{beam}}, A_{\text{det}}, A_{\text{overlap}}) \tag{4.13}$$

With A_{det} given by Equation. 4.11,

$$A_{\text{det}}(a) \tag{4.14}$$

And A_{overlap} given by Equation. 4.10,

$$A_{\text{overlap}}(a, r, \beta) \tag{4.15}$$

Where β is given by Equation. 4.5,

$$\beta(a, r) \tag{4.16}$$

And r is given by Equation. 4.2,

$$r(d_m, d_0, \theta) \tag{4.17}$$

Therefore,

$$P_{\text{det}}(P_{\text{beam}}, \theta, d_0, d_m, a) \tag{4.18}$$

The fit parameters for the analytical model are P_{beam}, θ, and d_0. The independent variable is d_m and a is a known value.

4.1.2.3 Misalignment

An additional simulation model was tested where the beam and detector were not assumed to be normal or centrally aligned. The beam area was then a conic section and the overlap area was calculated via surface integral. This model proved to have too many degrees of freedom to provide a unique fit to the experimental data.

4.1.2.4 Gaussian Model

The geometric analytical model assumes that the beam front has a uniform intensity whereas the intensity profile is better represented by a Gaussian intensity profile [14][15]. To compare the accuracy of the geometric analytical model, a Gaussian model is developed which implements a Gaussian beam intensity profile and propagation characteristics. The Gaussian beam intensity profile is given by,

$$I(r, d) = \frac{2P_{\text{beam}}}{\pi \cdot \omega(d)^2} \exp\left(-2\frac{r^2}{\omega(d)^2}\right) \tag{4.19}$$

Where r is the radial distance from the beam center, d is the distance from the beam

waist, and $\omega(d)$ is the beam radius at position d. The beam radius is defined as the distance from the beam axis where the intensity is $1/e^2$ the maximum value [REF?].

$$\omega(d) = \omega_0 \sqrt{1 + \left(\frac{d}{z_R}\right)^2} \tag{4.20}$$

Where z_R is the Rayleigh length defined as $z_R = \pi {\omega_0}^2/\lambda$, ω_0 is the beam waist, and λ is the wavelength. The power incident on the detector is then the surface integral of the intensity profile bounded by the detector dimensions.

$$P_{\text{det}} = \int_{-a}^{a} \int_{-a}^{a} I(r, d)\, dx\, dy \tag{4.21}$$

$$P_{\text{det}} = P_{\text{beam}} \operatorname{erf}\left(\frac{\sqrt{2}a}{\omega(d)}\right)^2 \tag{4.22}$$

Plugging in Equation. 4.20, the definition for z_R, and Equation. 4.1, the Gaussian fit parameters are shown.

$$P_{\text{det}}(P_{\text{beam}}, \omega_0, d_0, d_m, a, \lambda) \tag{4.23}$$

The Gaussian fit parameters are P_{beam}, ω_0, and d_0. The independent variable is d_m, and a and λ are known values.

4.1.3 Simulation Model

The simulation model is constructed using a point source. The source divergence and power are determined from fitting the analytical model to the experimental measurement. The detectors are logarithmically spaced from the detector to match the semi-logarithmic plot. The point source is placed at a distance d_0 from the first detector and given a divergence angle of θ. To demonstrate the effect of translational offset, x_0, the source is moved laterally relative to the detectors.

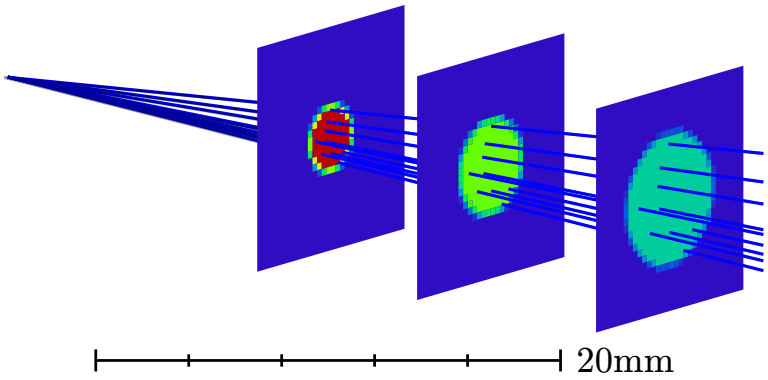

Figure 4.3: Simulated point source with three detectors.

4.2 Fiber Attenuation

The attenuation characteristics of the emissive fibers is desired. With the detector at a fixed radial distance to the fiber, it is moved along the length of the fiber. This is repeated with both the KSLD and Versalume fibers. The attenuation coefficient of the Versalume fiber is listed by the manufacturer and used as partial verification of experimental results.

The Versalume fiber is injected from a single end while the KSLD fiber is injected from both ends. As shown in Figure. 4.4, the reference point for the Versalume fiber is at the injection end while the reference point for the KSLD fiber is at the middle of the fiber length.

4.2.1 Experimental Setup

The fiber is affixed to a length of black powder coated aluminum extrusion with the portions not fixed to the extrusion being covered in light blocking material to minimize stray light. The power is measured using an automated script running in Matlab.

4.2.2 Analytical Models

The analytical model utilizes a simple fiber attenuation relation. The attenuation coefficient, α, is given in dBm/m. Power is written in both milliwatts (mW) and decibel-milliwatts (dBm), as denoted by the subscripts P_{mW} and P_{dBm}. The initial power P^0_{dBm} is the power at the origin in dBm. The distance from the origin is denoted by x which is in meters.

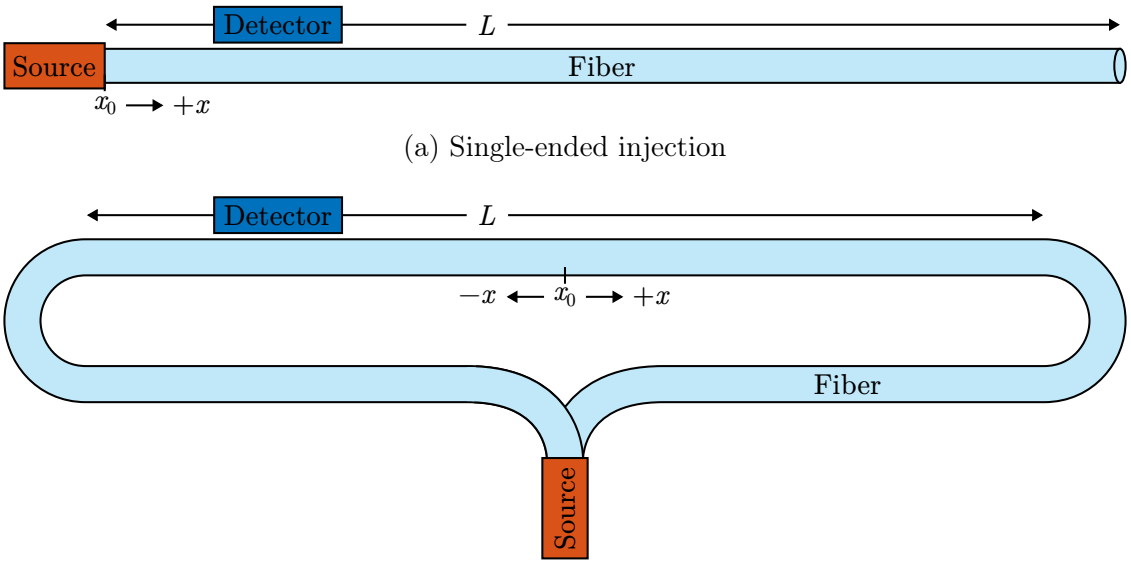

(a) Single-ended injection

(b) Dual-ended injection

Figure 4.4: Fiber attenuation setup schematics.

4.2.2.1 Single-Ended-Injected Model

The single-ended-injection model is simply the initial power minus αx dBm.

$$P_{\text{dBm}}(x) = P^0_{\text{dBm}} - \alpha(x - x_0) \tag{4.24}$$

4.2.2.2 Dual-Ended-Injected Model

The dual-ended-injected model accounts for the light traveling around the loop in both directions. As the origin is equally distant from either end of the fiber, then the attenuation is split between the two directions, denoted P^+ and P^-. The power at distance x from the longitudinal center of the fiber can then be derived as follows,

$$P^+_{\text{dBm}} = \left(P^0_{\text{dBm}} - \log_{10}(2)\right) + \alpha(x - x_0) \tag{4.25}$$

$$P^-_{\text{dBm}} = \left(P^0_{\text{dBm}} - \log_{10}(2)\right) - \alpha(x - x_0) \tag{4.26}$$

$$P^{+}_{\mathrm{mW}} = 10^{(P^{+}_{\mathrm{dBm}}/10)} \tag{4.27}$$

$$P^{-}_{\mathrm{mW}} = 10^{(P^{-}_{\mathrm{dBm}}/10)} \tag{4.28}$$

$$P_{\mathrm{mW}} = P^{+}_{\mathrm{mW}} + P^{-}_{\mathrm{mW}} \tag{4.29}$$

$$P_{\mathrm{dBm}} = 10 \log_{10} \left(P_{\mathrm{mW}} + P^{-}_{\mathrm{mW}} \right) \tag{4.30}$$

4.3 Radial Emissions

The radial emissions from a bare emissive fiber are measured to serve as a baseline for more complex optical systems and to explore some of the basic parameters relevant to the simulation environment. The detector's position is fixed in the lengthwise direction of the fiber while its radial distance from the fiber is varied.

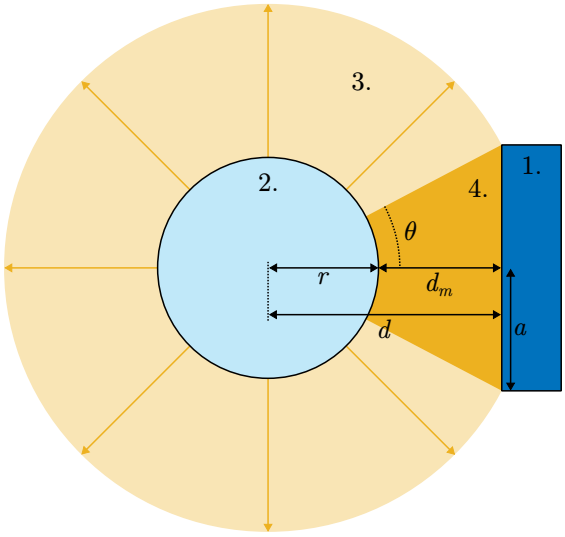

Figure 4.5: Cross sectional schematic of radial emission setup. 1. Detector, 2. Emissive fiber, 3. Radiated light, 4. Portion of radiated light incident on the detector.

Three variations of the setup are explored, the minimal radial model, the mirror-surface model, and the Lambertian-surface model. The minimal radial model is comprised of only an emissive fiber while the mirror-surface and Lambertian-surface models have an additional surface placed behind the fiber.

4.3.1 Experimental Setup

To measure radial fiber emission, the fiber is mounted to a Type-II matte-black anodized machined aluminum mounting joist from Thorlabs. The joist provides a flat light-absorbing surface on which to hold the fiber for testing. The detector is placed on a translation stage which is mounted to a 50 cm long optical rail assembly. The translation stage allows for high-resolution short-distance radial measurements while the translation stage is used for low-resolution long-distance radial measurements.

The experiment is conducted for the white (450 nm) and IR (850 nm) outputs of the KSLD Tx module, both with the KSLD emissive fiber.

4.3.2 Analytical Model

Two analytical models are developed to parameterize the optical system. The difference between the two models is whether the surface that the fiber is mounted to is accounted for. In the minimal radial model, the fiber is assumed to be floating in space with none of the surroundings having any effect. In the mirror-surface and Lambertian-surface models, an attempt is made to include the surface that the fiber is affixed to.

As described in Section 4.3.3, three models, two of which poses an added back surface are simulated. The surface is set as a perfect mirror in one case and as a Lambertian scattering surface in the other. In the corresponding analytical models, the scattering of the reflected light from the surfaces back through the fiber is ignored. These models are intended only to serve as guides for the qualitative characteristics that are expected from the simulation models, such as the increased directivity of the mirror-surface model relative to the Lambertian-surface model. The two surface models demonstrate the two extremes of adding a back surface. to investigate if a back surface is needed to accurately simulate the radial system. The analytical models then serving as a confirmation that the core mechanics of the optical system are understood. Ultimately, only the minimal radial analytical model is used to fit to the experimental data as the mirror-surface model contains too many parameters

given the experimental dataset and the Lambertian-surface model is incomplete.

In both models, the fiber is assumed to radiate uniformly radially. Additionally, a distance offset d_0 is not included in Figure. 4.5 but is included in the analytical model. d_0 is used to account for experimental error in the distance measurement zero-point. This is needed as the actual detector surface is inset into the detector housing by 1 mm to 2 mm. Additionally, the detector is not placed in direct contact with the fiber to avoid damage.

$$d = d_m + d_0 \tag{4.31}$$

Note that the system is treated as a 2D cross section of the fiber. The 2D model can be used to represent the 3D system as the portion of light captured is independent of length so long as the output power, P_{output}, is taken over the same length. The following power values are thus taken as power per unit length, where the unit length is the length of the detector, here that is 9.9 mm.

4.3.2.1 Minimal Radial Model

In the minimal radial model, the detected power, P_{det}, is proportional to the subtended angle of the detector to the fiber, θ, as seen in Figure. 4.5.

$$\frac{P_{\text{det}}}{P_{\text{output}}} = \frac{\theta}{\pi} \tag{4.32}$$

The subtended half-angle, θ, can be expressed in terms of detector height, a, and radial distance, d.

$$\theta = \tan^{-1}\left(\frac{a}{d}\right) \tag{4.33}$$

Equations 4.32 and 4.33 are used to derive an expression for P_{det} in terms of a and d.

$$P_{\text{det}} = P_0 \frac{\theta}{\pi} \tag{4.34}$$

$$P_{\text{det}} = P_0 \frac{\tan^{-1}\left(\frac{a}{d}\right)}{\pi} \tag{4.35}$$

4.3.2.2 Mirror-Surface Model

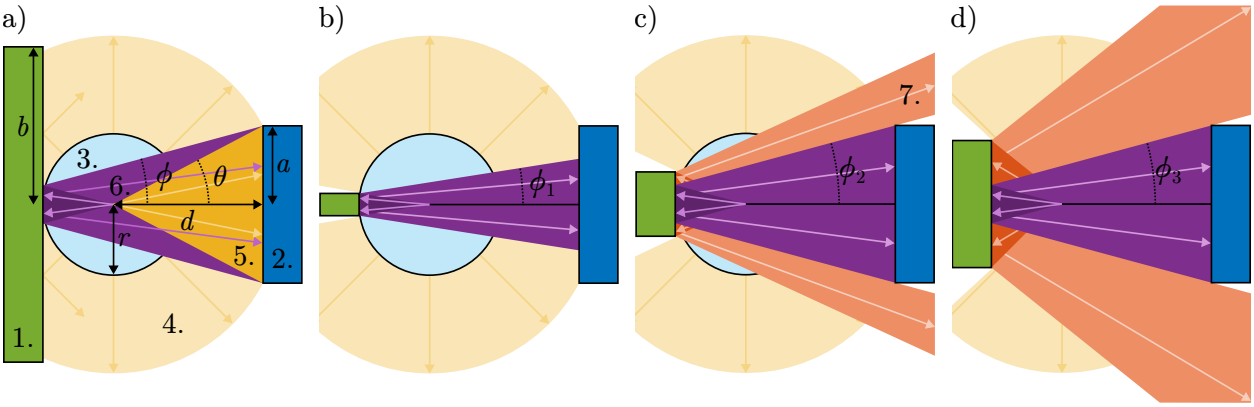

(a) Complete model (b) Small surface (c) Medium surface (d) Large surface

Figure 4.6: Cross sectional schematic of radial emission setup with added mirror surface. 1. The mirror surface. 2. The detector. 3. The emissive fiber. 4. The radiated light. 5. The portion of radiated light directly incident on the detector. 6. The portion of radiated light that is incident on the mirror surface then reflected into the detector. 7. The portion of radiated light that is incident on the mirror surface but is not incident on the detector.

As visualized in Figure. 4.6, the mirror-surface model can be broken into two parts. The first part is the portion of light that is directly incident on the detector. This will be the same as the minimal radial model seen in Section. 4.3.2.1. The second part is the portion of light that is incident on the mirror-surface before being reflected into the detector. It can be treated similarly to the minimal radial model except for that the path length will be longer by twice the distance from the fiber to the mirror-surface. Here that distance is twice the

radius of the fiber, r, as seen in Figure. 4.6a. θ and ϕ can then be written as follows,

$$\theta = \tan^{-1}\left(\frac{a}{d}\right) \tag{4.36}$$

$$\phi = \tan^{-1}\left(\frac{a}{d+2r}\right) \tag{4.37}$$

$$\tag{4.38}$$

P_{det} is then the combined power from these two portions of the total emitted light.

$$P_{\text{det}} = P_0\frac{\theta+\phi}{\pi} \tag{4.39}$$

However, Equation. 4.39 is only true in the case where the back surface is sufficiently large. As an example, compare ϕ_1, ϕ_3, and ϕ_3, from Figures. 4.6b, 4.6c, and 4.6d respectively.

$$\phi_1 < \phi_2 = \phi_3 \tag{4.40}$$

In Figure. 4.6a, the subtended angle of reflected light is limited by b. As b increases, ϕ will increase up until a point, b_{crit}, above which increasing b will have no effect. This can be observed in Figures. 4.6c and 4.6d.

$$b_{\text{crit}} = \frac{a(d+2r)}{d} \tag{4.41}$$

$$\phi = \begin{cases} \tan^{-1}\left(\frac{b}{r}\right) & \text{if } b < b_{\text{crit}} \\ \tan^{-1}\left(\frac{a}{d+2r}\right) & \text{if } b \geq b_{\text{crit}} \end{cases} \tag{4.42}$$

Equation. 4.42 is then the complete expression for ϕ and is used in Equation. 4.39.

4.3.2.3 Lambertian-Surface Model

The Lambertian-surface model is similar to the mirror-surface model in that the portion of power directly incident on the detector will be the same as in the minimal radial model.

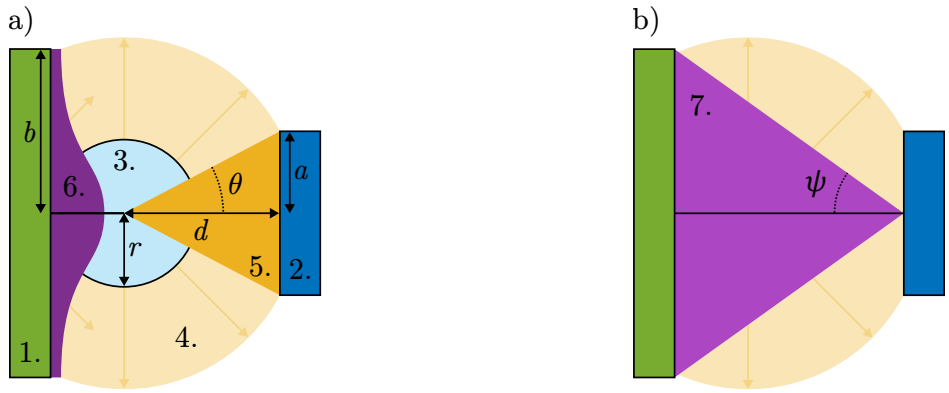

(a) Back-Surface irradiance (b) Back-surface radiance

Figure 4.7: Cross sectional schematic of radial emission setup with added Lambertian surface. 1. The Lambertian surface. 2. The detector. 3. The emissive fiber. 4. The radiated light. 5. The portion of radiated light directly incident on the detector. 6. The irradiance incident on the Lambertian surface. 7. The subtended angle of the Lambertian surface to the detector.

In contrast to the mirror-surface model, the light incident on the back surface will be diffusely reflected. Thus, instead of finding the subtended angle of the reflected portion, the Lambertian surface is treated as a diffuse source and the subtended angle of the Lambertian surface to the detector is used as a metric of radiance, as seen in Figure. 4.7b. However, the irradiance from the Lambertian surface will not be uniform across the surface as the fiber is treated as a point source and the radiance on the Lambertian surface will drop off via the inverse-square law.

Without solving the entire radiometric problem, some of the qualitative effects of the change from a mirror finish to a Lambertian finish can be discussed. The expression for the subtended Lambertian surface angle, ψ, is given,

$$\psi = \tan^{-1}\left(\frac{b}{d+r}\right) \tag{4.43}$$

Compared to the minimal radial model, the Lambertian surface model will result in a higher detected power for the same output power as the effect of the back surface is additive. However, as the reflected light is not directional, the detected power is expected to be lower

than for the mirror-surface model.

4.3.3 Simulation Model

The simulation model is constructed of the emissive fiber model described in Section. 3.2.6.2, with detectors placed radially. The spacing between the detectors is logarithmic.

Unless stated otherwise, the default length of the simulated fiber is 71.2 mm, which is the length of the segment of mounted fiber in the experimental setup. Similarly, the default simulated fiber radius is 1 mm, which is the measured radius of KSLD fiber.

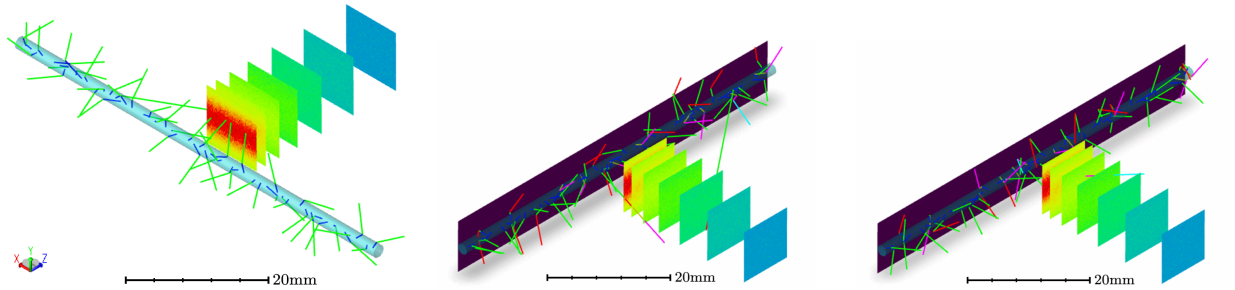

(a) Minimal radial model (b) Mirror-surface model (c) Lambertian-surface model

Figure 4.8: Isometric view of simulated radial emission models in Zemax.

To better simulate the experimental system, a reflective surface behind the fiber is added to the radial model. The simulation model can be seen in Figure. 4.8. Two different surfaces are explored, a mirror surface and a diffuse surface with Lambertian scattering.

4.4 Radial Emissions with Added Reflector

The radial fiber emissions are simulated with the addition of a parabolic reflector. Along with providing another point of comparison for the simulation environment, the goal is to determine the parabolic reflector's effectiveness and possible optimizations parameters.

A point source placed at the focus of parabolic reflector will result in parallel rays. As the rays do no converge or diverge, the system's performance will be less dependent on the distance between the fiber and detector. By placing collecting optics before the receiver the parallel rays can be focused onto the detector to maximize the amount of detected power.

Figure. 4.9, shows some of the parameters relevant to the parabolic reflector setup. The semi-latus rectum ℓ is equivalent to the radius of curvature parameter given by Zemax for conic objects. The distance from the back of the reflector to the focus is given by f. f and ℓ are related by,

$$\ell = 2f \tag{4.44}$$

The distance between the reflector and the fiber is,

$$f = g + r \tag{4.45}$$

Where r is the fiber radius. The depth of the reflector D is related to the reflector aperture A via the parabolic equation,

$$A^2 = 4fD \tag{4.46}$$

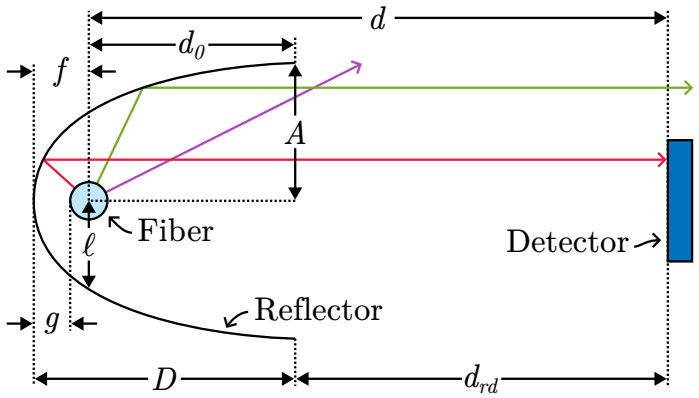

Figure 4.9: Parabolic reflector setup and parameters.

The distance between the fiber center and the detector is denoted d for consistency. The distance between the edge of the reflector and the detector is denoted d_{rd}. The distance from the fiber center to the reflector edge, also known as the distance offset, is given by d_0.

4.4.1 Experimental Setup

The KSLD emissive fiber is placed in the KSLD parabolic reflector and the radiated power is measured at various radial distances. The experiment is repeated for both the KSLD White

and KSLD IR sources.

4.4.2 Simulation Model

The radial fiber model described in Section. 4.3.3 is employed with an additional parabolic reflector with the dimensions shown in Figure. 3.3. The reflector is simulated with a mirror surface.

4.4.3 Elliptical Reflector

An elliptical reflector is a possible alternative when the distance between the fiber and detector does not very by a large degree. An elliptical reflector will focus rays originating from one focus to the opposite focus. If the fiber is placed at one focus, and the detector at the other, the elliptical reflector will focus the light from the fiber to the detector.

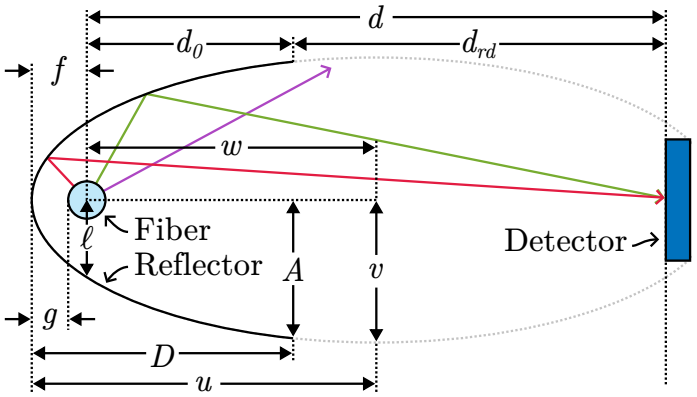

Figure 4.10: Elliptical reflector setup and parameters.

In Figure. 4.10, the setup and parameters can be seen. The parameters are similar to those of the parabolic reflector as they are both conic sections, however, they are not equivalent. For an ellipse, the semi-lactus rectum, ℓ, is given by,

$$\ell = \frac{v^2}{u} \tag{4.47}$$

The aperture A is related via,

$$A = a\sqrt{1-e^2} = a\sqrt{K+1} \tag{4.48}$$

Where u is the semi-major axis and v is the semi-minor axis of the ellipse. By changing the conic constant $K = -e^2$, where e is the linear eccentricity, the focal length w is modified. Thus the radius of curvature cannot be changed without changing either the aperture or the focal length.

$$e = \frac{w}{u} = 1 - \frac{g-r}{u} \tag{4.49}$$

4.5 Radial Emissions with Added Reflector and Lens

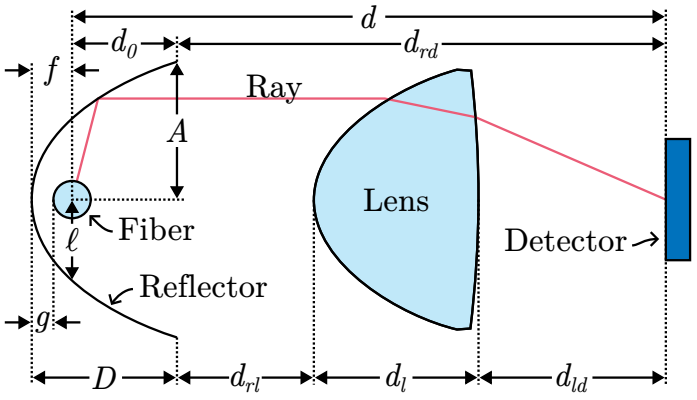

Figure 4.11: Collection optics setup parameters.

4.5.1 Setup Configurations

In Figure. 4.11, the setup parameters are shown. A detailed description of the parabolic reflector parameters and their relations can be found at the beginning of Section. 5.4. The distance d is defined as the distance between the fiber center and the detector for consistency. The distance between the fiber center and the edge of the reflector is the offset distance d_0. The distance between the reflector and the lens is given by d_{rl}. The distance taken by the lens thickness is given by d_l. The distance between the back surface of the lens and the detector is given by d_{ld}. The distance between the reflector edge and the detector is denoted

d_{rd}.

4.5.1.1 Experimental Setup

The experimental setup utilized the parabolic reflector from Section. 5.4 and the condenser lens and spectral filters from Section. 3.1.5 as well as the KSLD IR and KSLD White sources with the KSLD emissive fiber and the power meter from Section. 3.1.6. The setup was places in a blackout box to prevent stray light from being measured as the detected power level was low. The detector is placed directly behind the condenser lens and the power is recorded as it is moved away from the lens. We expect to see a peak that corresponds to the focus of the condenser lens.

4.5.2 Simulation Model

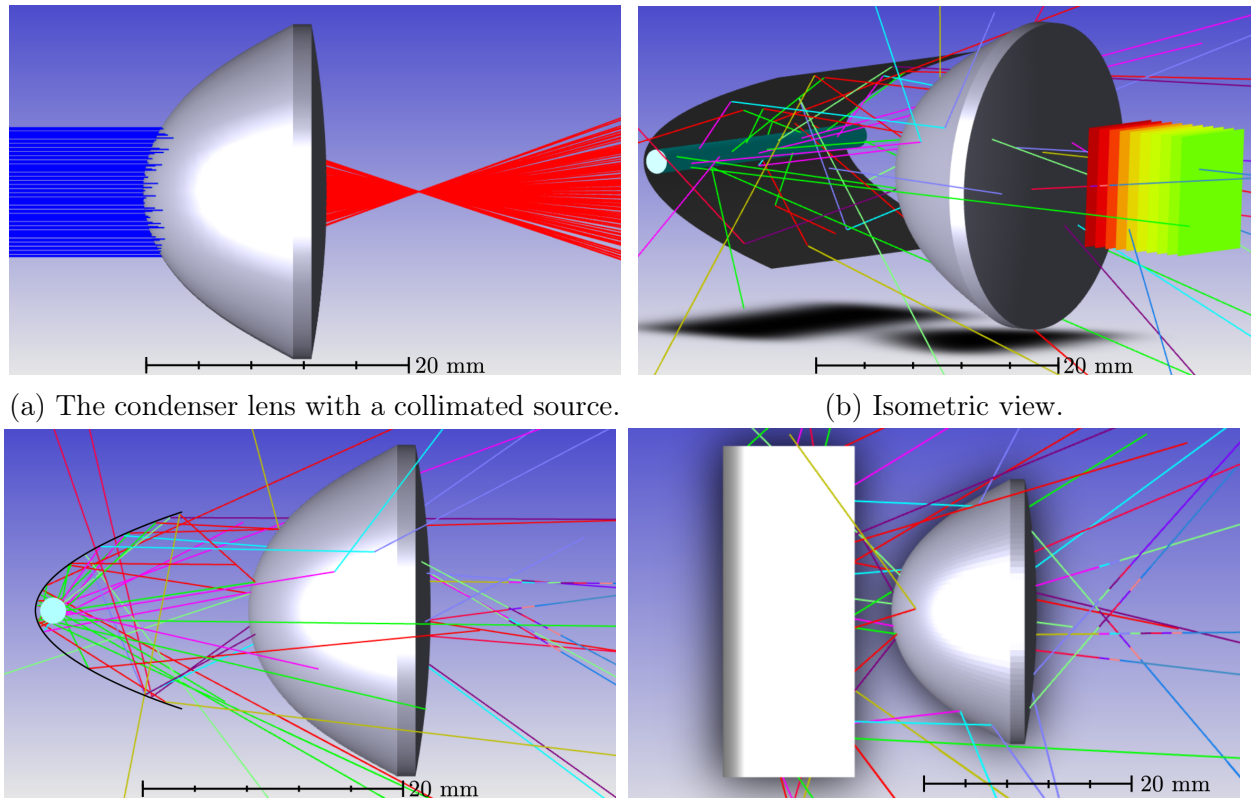

(a) The condenser lens with a collimated source.

(b) Isometric view.

(c) YZ-plane view.

(d) XY-plane view.

Figure 4.12: Zemax simulation of the condenser lens and the full optics setup.

The emissive fiber model and parabolic reflector geometry described in previous sections

is used with the addition of a condenser lens whose parameters are imported from Thorlabs' lens catalog. In Figure. 4.12a, the function of the simulated condenser lens with a collimated beam is shown. The effective focal length of the condenser lens is 16 mm which results in a back focal length of roughly 8 mm. The full simulation setup is shown in Figures. 4.12b, 4.12c, and 4.12d. Because of the diffuse source, it is difficult to see the effect of the condenser lens.

Results and Discussion

5.1 Calibration

Using the automated acquisition setup, two sets of data were recorded for the baseline red laser and FC/APC connector setup and four sets of data were recorded for the KSLD IR and FAKRA connector setup.

Parameter	Baseline	KSLD IR
P_0 [mW]	0.479	61.6
d_0 [mm]	9.55	10.2
θ [deg]	5.13	21.2
x_0 [mm]	1.75	1.00

Table 5.1: Point source simulation parameters.

Data from each configuration were aggregated then used to fit the analytical model to determine the subsequent simulation model parameters. Additionally, both configurations were simulated with some translational offset, x_0. In Figure. 5.1, the experimental data, analytical fit, simulated data, and simulated data with translational offset are plotted.

In Figure. 5.1, strong agreement between the experimental data, analytical fit, and simulation data is demonstrated. The analytical fit and simulation data produce nearly identical results which indicates agreement in an idealized environment.

5.1.1 Beam Offset

The simulation data with translational offset shows improved agreement with the experimental data. However, as discussed in Section. 4.1.2.3, the analytical model that accounts for misalignment between the beam and detector is over-fitted and thus cannot be used to determine the translational offset and other alignment parameters. The simulation data with translational offset is a demonstration of the qualitative effect of misalignment. The type

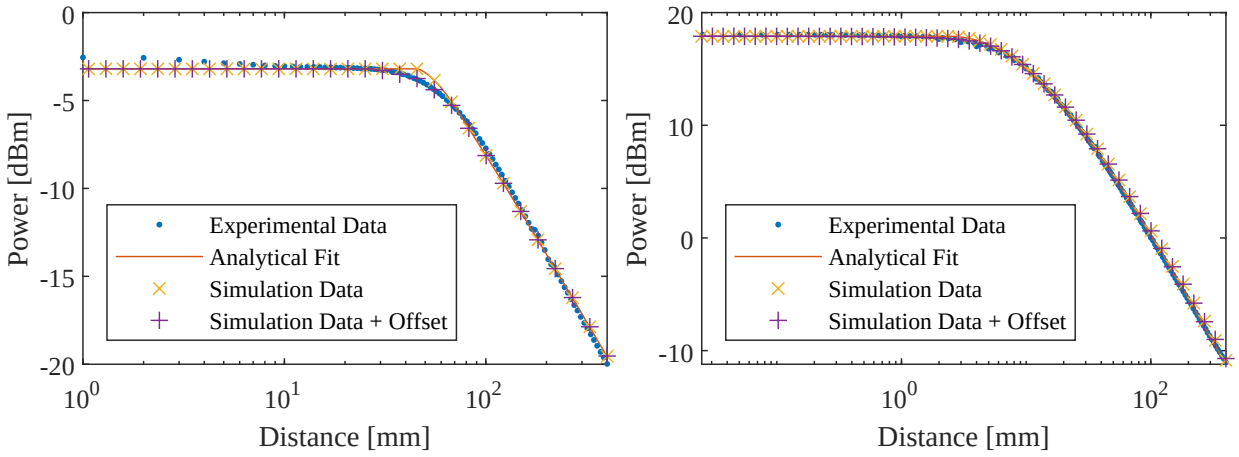

(a) Baseline red (635 nm) source with FC/APC connector.

(b) KSLD IR (850 nm) source with FAKRA connector.

Figure 5.1: Comparison of source power models.

and quantity of misalignment is not known however the qualitative characteristics fit the observed differences between the experimental data and the analytical model from Section. 4.1.2.

5.1.2 Beam Divergence

As a final measure of the analytical model, the beam divergence was measured experimentally for the KSLD IR setup. The experimental divergence was found to be $22.5° \pm 5°$ which is in agreement with the fitted value of 21.2°.

5.1.3 Gaussian Model

The Gaussian model is fitted to the experimental data and the root-mean-square error (RMSE) is calculated. The Gaussian analytical model is found to have an RMSE of 0.180 dBm for the baseline red source and 0.140 dBm for the KSLD IR source while the geometric model has an RMSE of 0.303 dBm for the baseline red source and 0.148 dBm for the KSLD IR source. The Gaussian model performs better than the geometric model, however, the difference between the two models is not substantial and the geometric model is found to provide an acceptable approximation of the physical system. As the purpose of the analytical model is the provide a translation layer between the physical system and the simulated system, and

the Gaussian model is incompatible with the simulation model, the geometric model's use is validated in this setup and in further setups.

5.2 Fiber Attenuation

The attenuation rate was measured by recording the optical power received by a detector at a fixed radial distance from the fiber as it is translated longitudinally over the length of the fiber, Figure. 4.4.

Three fiber and source combinations were measured; the baseline red laser with the Versalume emissive fiber, and the KSLD source and KSLD emissive fiber for both white (450 nm) and IR (850 nm) optical outputs.

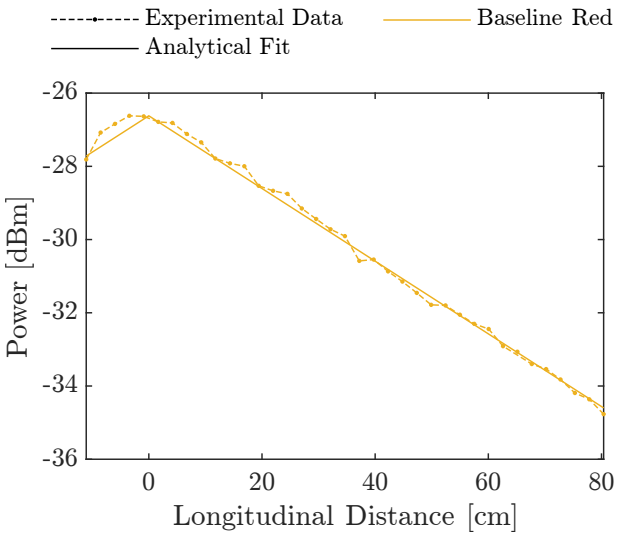

Figure 5.2: Detected power from Versalume emissive fiber with baseline red (635 nm) optical source.

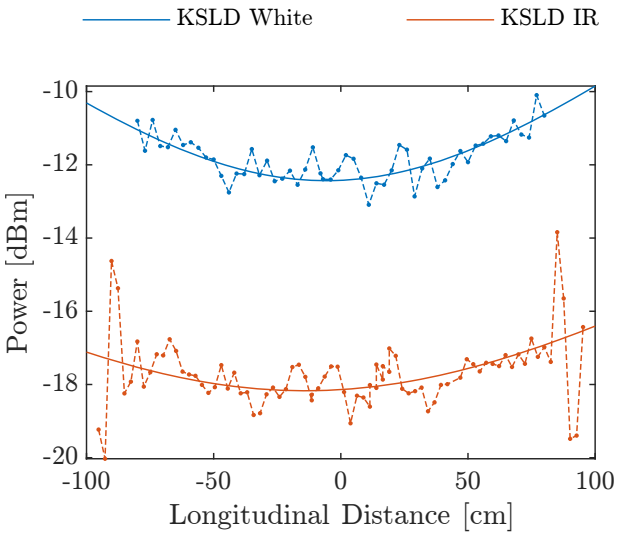

Figure 5.3: Detected power from KSLD emissive fiber with KSLD White (450 nm) and KSLD IR (850 nm) optical sources.

Parameter	KSLD White	KSLD IR	Baseline Red
P_0 [dBm]	-12.43	-18.17	-26.62
P_0 [nW]	57.11	15.24	2.178
x_0 [cm]	-35.75	83.7	11.1
α [dBm/m]	4.935	3.669	9.925

Table 5.2: Fiber attenuation fit parameters.

The Versalume fiber results are compared to the manufacturer listed attenuation coefficient of 10 dBm/m. The experimental value of 9.925 dBm/m has a percent error of 0.75%.

5.2.1 Emission Characteristics

The KSLD emissive fiber was found to have high local emission variability as demonstrated in Figure. 5.4. To ensure that the variability was not due to an error in measurement methodology, the same portion of fiber was measured twice at two different resolutions R, 1 cm and 0.1 cm, shown in blue and orange respectively.

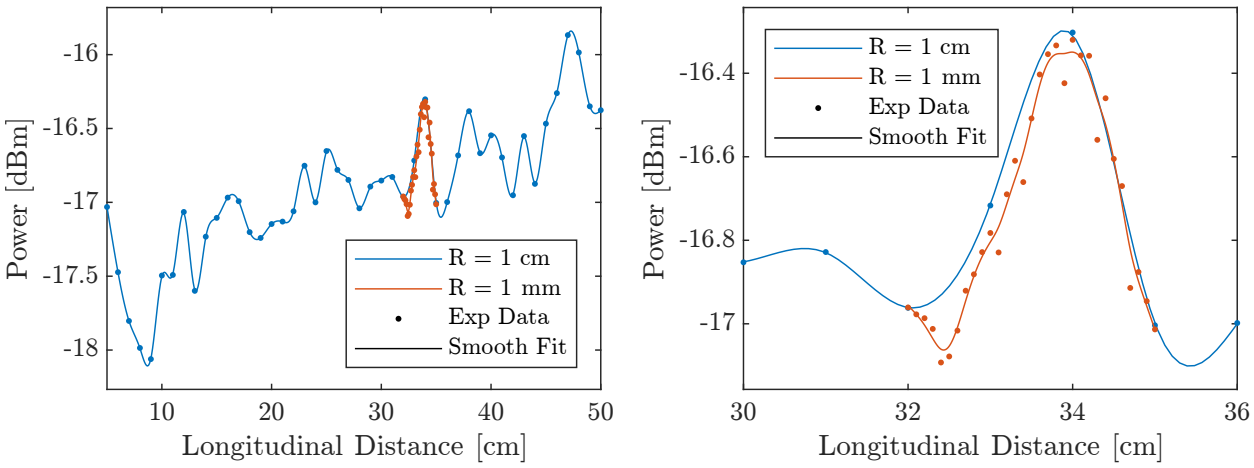

(a) Full 1 cm measurement range.

(b) Reduced 1 mm measurement range.

Figure 5.4: High resolution measurement of detected power from KSLD emissive fiber with KSLD IR source (850 nm) and KSLD emissive fiber.

In Figure. 5.4b, a variation of over 0.6 dBm is seen in less than 1 cm. This is equivalent to an attenuation coefficient of over 60 dBm/m. Thus with the KSLD fiber a small change in alignment between the fiber and the detector may result in a large change in optical signal strength. The same local variability was not seen with the Versalume fiber as observed in Figure. 5.2.

5.3 Radial Emissions

In an effort to assert that the simulated emissive fiber behaves as expected, two core simulation parameters are tested with the minimal radial model; the fiber radius and the fiber

length. The simulation models with added back surfaces are explored and the results from all three simulation models are compared to experimental data.

5.3.1 Effect of Varying Fiber Radius

The first simulation result is performed as a sanity check. The radius of the fiber is swept and the power as a function of distance is measured. The expectation, as can be seen in the analytical model of Section. 4.3.2.1, is that the radius will have no effect.

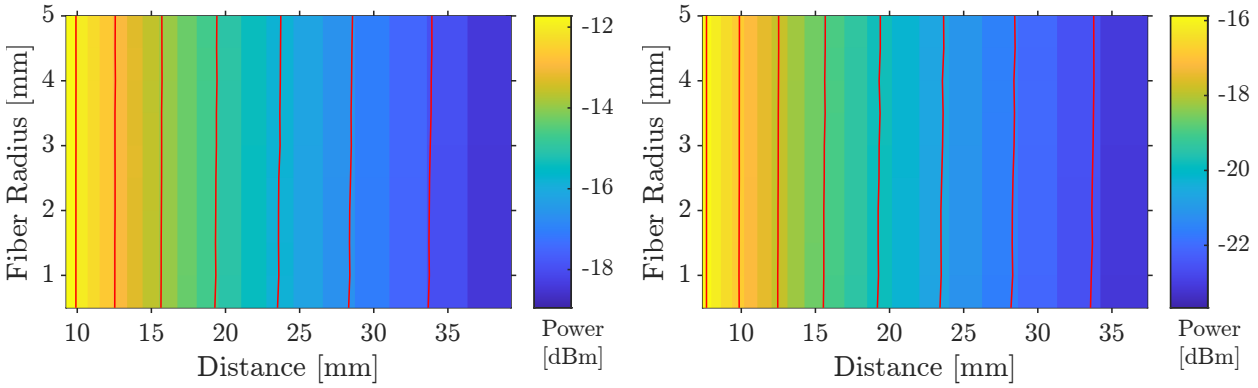

(a) KSLD White (450 nm) (b) KSLD IR (850 nm)

Figure 5.5: Simulated effect of fiber radius with minimal radial model.

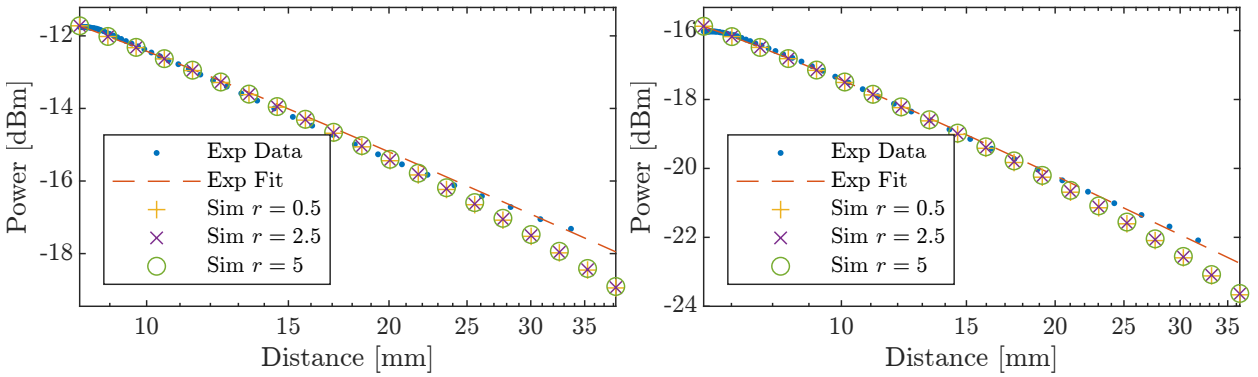

(a) KSLD White (450 nm) (b) KSLD IR (850 nm)

Figure 5.6: Comparison of minimal radial model with varying fiber radius, r, and the associated experimental data and analytical fit.

It can be seen in Figure. 5.5, that the radius of the fiber is independent from the received power at the detectors as the received power is constant across all fiber radii for a given distance.

In Figure. 5.6, the simulation results for select fiber radii are plotted against the experimental data and the associated analytical fit. Strong agreement between the experimental data and the analytical fit are observed. The simulation results show strong agreement over short distances, but the rate of decay is steeper than in the experimental data. Parameters which may account for this difference are explored in further sections.

5.3.2 Effect of Varying Fiber Length

The analytical model assumes uniform radiation from the fiber. In an ideal simulation, the entire length of the emissive fiber would be simulated. However, this would be computationally inefficient as the vast majority of the light would not be incident on the detector. The probability of a ray hitting a detector is higher the closer to the detector a ray originates and drops off via the inverse-square law as the distance grows.

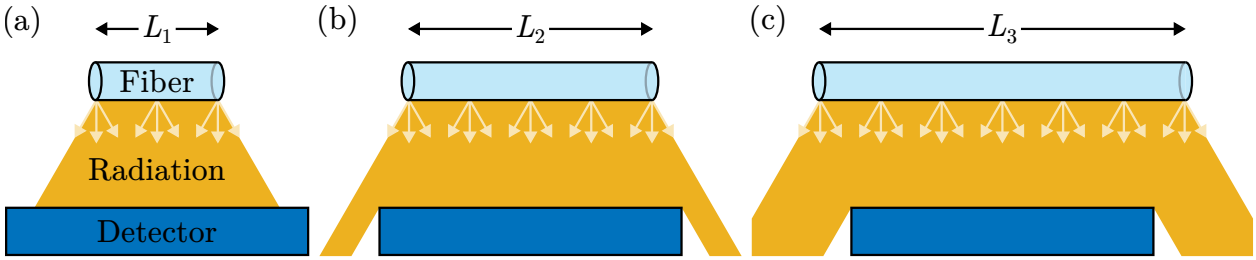

Figure 5.7: Simplified diagram on the effect of simulated fiber length.

In Figure. 5.7, a simplified model of the radiation from fibers of three lengths is shown. In the simplified model, the shortest fiber does not produce radiation that is uniform across the length of the detector. Simulating only a small portion of fiber closest to the detectors will result in the most efficient simulation. Determining how the simulated fiber length affects the radiation characteristics, is thus important to determine the best use of computational resources.

Varying the fiber length will also demonstrate the emission characteristic of large diffuse sources, namely that for a constant initial power, the rate of decay in received power at the detector as a function of distance is decreased. This is due to the subtended angle of the source from the perspective of the detector.

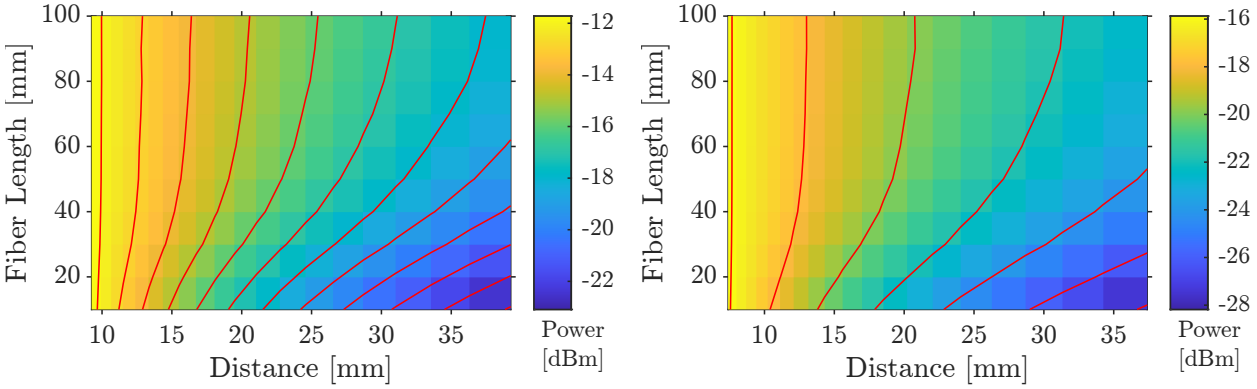

(a) KSLD White (450 nm) (b) KSLD IR (850 nm)

Figure 5.8: Simulated effect of fiber length with minimal radial model.

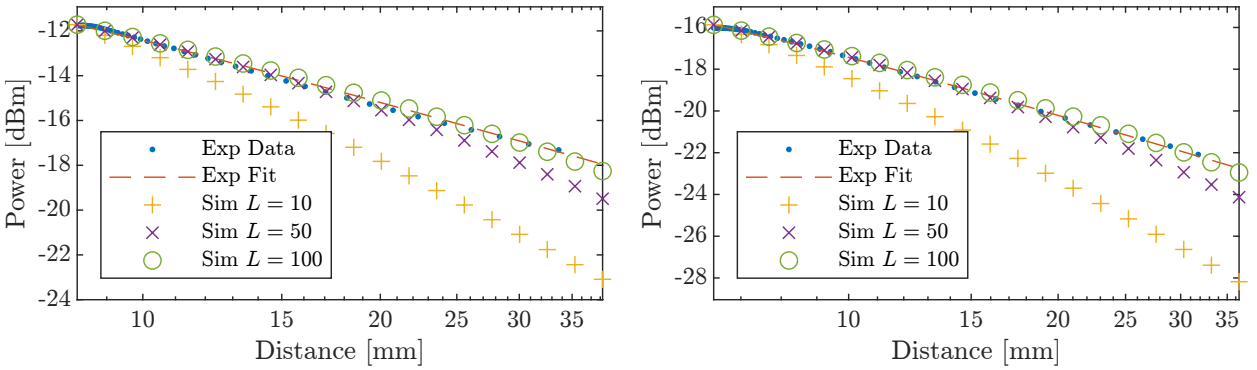

(a) KSLD White (450 nm) (b) KSLD IR (850 nm)

Figure 5.9: Comparison of minimal radial model with varying fiber length, L, and the associated experimental data and analytical fit.

In Figure. 5.8, the reduced rate of decay for larger diffuse sources is clearly visible. Note that the rate of decay is larger for small fiber lengths. This is because of the inverse effect where the subtended angle of the detector to the fiber decays faster and is more important for shorter fibers.

In Figure. 5.9, the longest simulated fiber is seen to be closest to the experimental results and analytical fit. An alternative explanation is that a reflection from the fiber in the experimental results is significantly large. In the experimental setup the fiber is mounted onto a solid surface. The effect of this surface is not simulated and may be the source of the reflection.

A takeaway from these results is that the default fiber length value of 71.2 mm, taken

from the physical setup, is likely appropriate at producing the radiation characteristics seen in the experimental results.

5.3.3 Added Back Surfaces

To better simulate the experimental system, a reflective surface behind the fiber is added to the radial model. The simulation model can be seen in Figure. 4.8. Two different surfaces are explored, a mirror surface and a diffuse surface with Lambertian scattering.

To highlight the effect and characteristics of the added surfaces, the effect of surface height on received power as a function of detector distances is investigated.

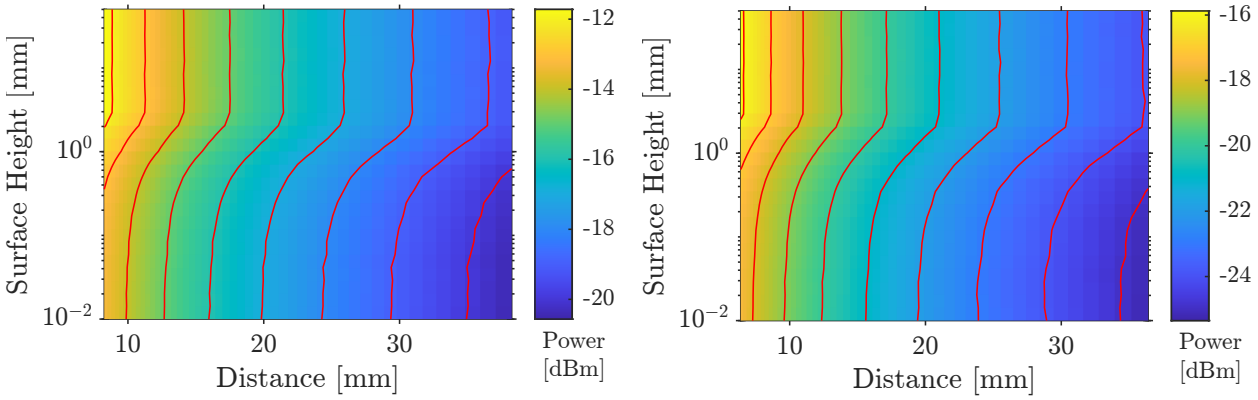

(a) KSLD White (450 nm) (b) KSLD IR (850 nm)

Figure 5.10: Simulated effect of back surface height with mirror-surface model.

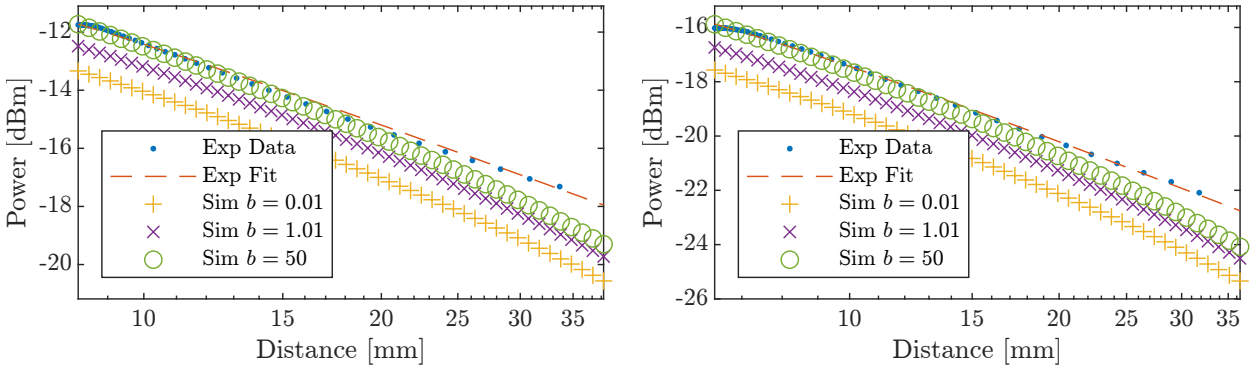

(a) KSLD White (450 nm) (b) KSLD IR (850 nm)

Figure 5.11: Comparison of mirror-surface model with varying back surface height, b, and the associated experimental data and analytical fit.

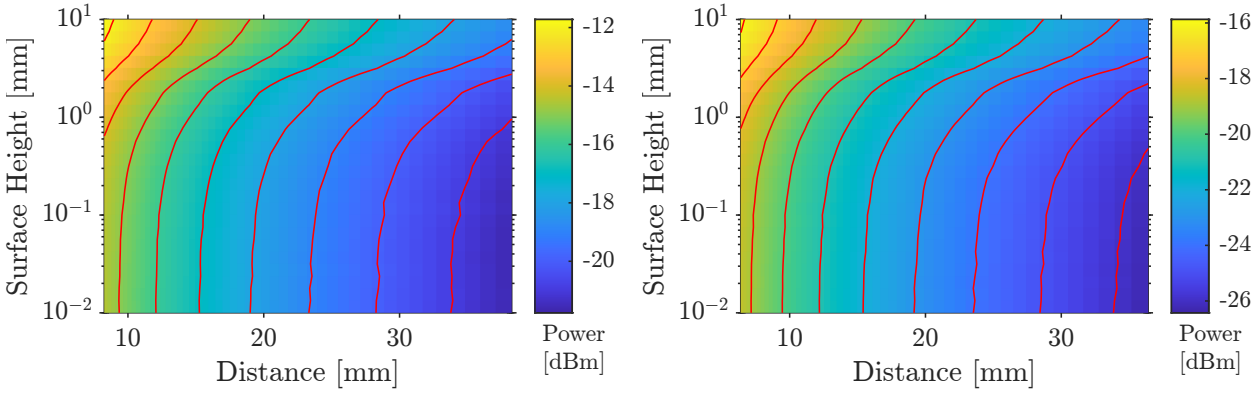

(a) KSLD White (450 nm) (b) KSLD IR (850 nm)

Figure 5.12: Simulated effect of back surface height with Lambertian-surface model.

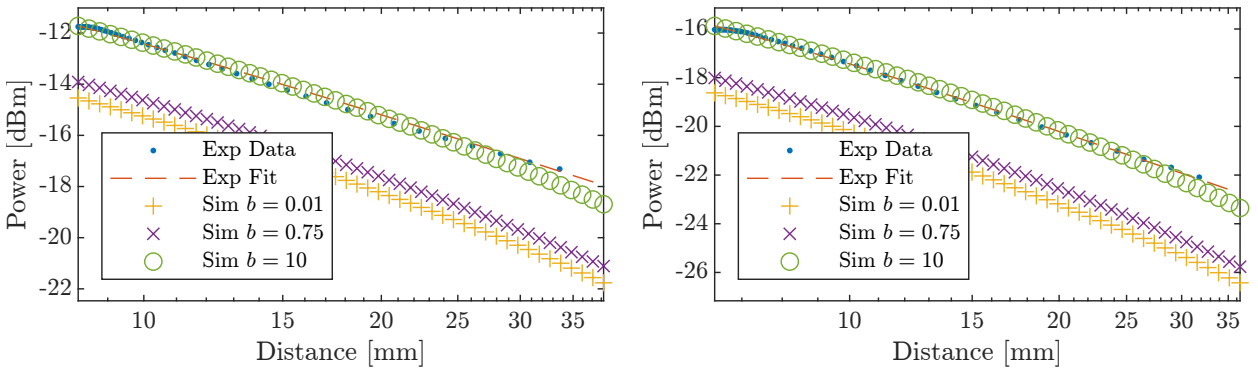

(a) KSLD White (450 nm) (b) KSLD IR (850 nm)

Figure 5.13: Comparison of Lambertian-surface model with varying back surface height, b, and the associated experimental data and analytical fit.

Instead of normalizing the received power across the sweep variable, as was done with the fiber radius and fiber length sweeps, the source power is kept constant. Because of this, the relative efficiencies of the different configurations can be observed.

In Figure. 5.10, the effects described in Section. 4.3.2.2 are seen. As the surface height increases, the subtended angle of the reflected light increases and so does the received power up until a point. In Figure. 5.12, it is seen that near $b = 3$ mm, the received power plateaus as the extra reflected light is no-longer incident on the detector.

For the diffuse Lambertian surface, Figure. 5.12 does not have any plateau as is expected from the analytical model described in Section. 4.3.2.3. Instead, the received power continues to increase as the surface height increases and the subtended angle to the detector increases.

5.3.4 Model Comparison

The three simulation models are compared to determine the sensitivity of the measurement setup and what level of detail must be achieved in simulation to produce accurate results.

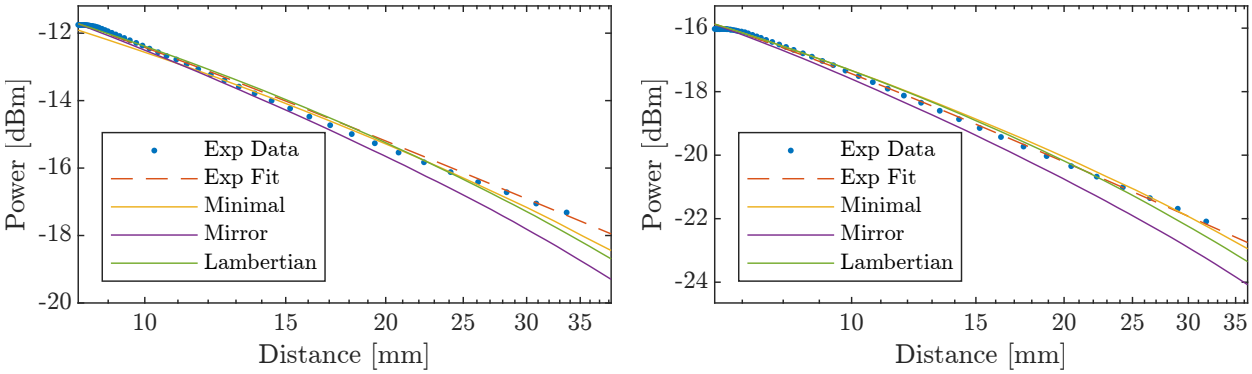

(a) KSLD White (450 nm) (b) KSLD IR (850 nm)

Figure 5.14: Radial model comparison.

In Figure. 5.14, the three models are compared against the experimental data and analytical fit. Of the three simulation models the diffuse surface model is closest to the experimental results. The minimal radial model performs better than the mirror surface model because of the divergence of reflected rays at large distances. The results are consistent with the physical back surface used in the experimental setup.

Despite these differences, all radial models perform an adequate job of simulating the physical system, especially at smaller distances. As the distances relevant to the intended application are relatively small, below 10 cm, the simplest model can be used to simulate the emissive fiber. This indicates that measurements are not particularly sensitive to environmental factors such as mounting the fiber on a surface.

The discrepancy with the simulation models at large distances is suspected to be due to ambient light. When the detector is close to the fiber the mounting surface will block ambient light from being detected, as the detector moves further away less ambient light will be blocked and more will be detected. This phenomenon is outside of the analytical model and would not be corrected by zeroing the detector prior to measurement.

5.4 Radial Emissions with Added Reflector

A number of parameters are explored in relation to an added reflector's effect on the amount of detected radial emissions. The radial emission characteristics of the simulation results and experimental results is compared. The sensitivity of the fiber placement in the parabolic reflector is simulated, and an initial exploration of the parameter space for the parabolic and elliptical reflectors is performed.

5.4.1 Fiber Placement in the Reflector

In order to achieve parallel rays from the parabolic reflector, the fiber must be placed at the reflector's focus. As the fiber cannot be suspended in mind-air, the location of the fiber will be dictated by the radius of the fiber. This means that the parabolic reflector geometry must be selected such that the gap g between the cusp of the parabola and the focus is equivalent to the fiber radius, Figure. 4.11. To demonstrate the effect of having the fiber outside of the focus of the parabolic reflector, simulations are conducted where the gap between the cusp of the parabola and the fiber is varied.

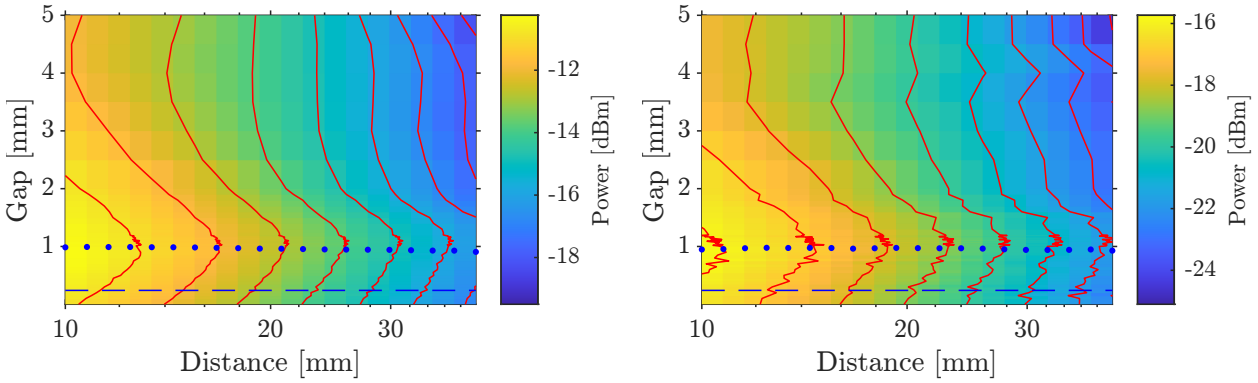

(a) KSLD White (450 nm) (b) KSLD IR (850 nm)

Figure 5.15: Simulated radial emissions as a function of reflector to fiber gap and detector distance.

In Figure. 5.15, the relationship between the received power, distance, and gap between the parabola and the fiber is shown. The fiber radius is 1 mm and the theoretical parabolic reflectors focus is 0.24 mm, shown as a blue dashed line. The maximum received power for

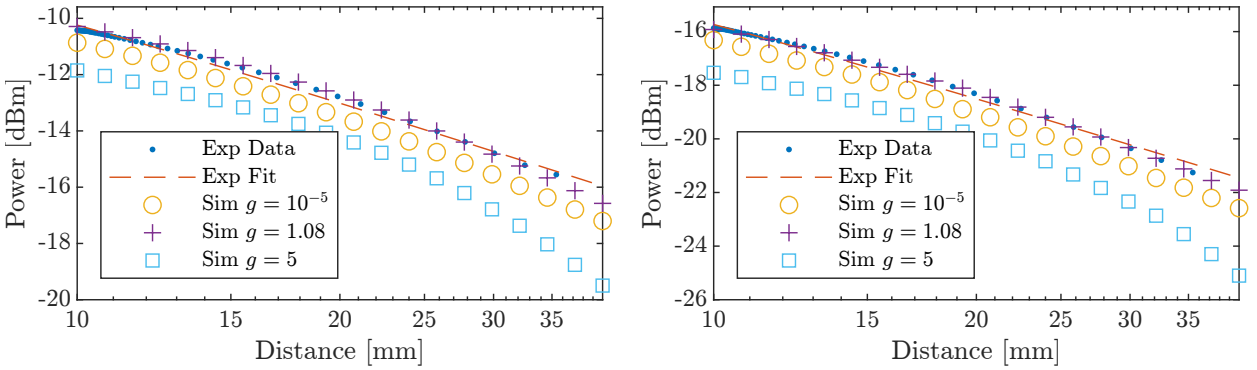

(a) KSLD White (450 nm) (b) KSLD IR (8500 nm)

Figure 5.16: Comparison between simulated results from systems with reflector to fiber gap, g, and experimental data and its fit.

each distance is plotted as blue dots.

As expected, the maximum does not occur at the theoretical focus of the parabolic reflector but at a larger gap size near 1 mm. By placing the source out of focus, the parabolic reflector will focus the light to the detector. As there are no collecting optics in this simulation, the maximum occurs when the focus from the reflector is at the detector.

This type of effect could be used to eliminate the need for collecting optics if the distance between the fiber and detector is keep constant. It should also be noted that unlike an elliptical reflector, parabolic reflectors will not produce an ideal focus when operated in this manner.

5.4.2 Parabolic Reflector Depth

The emission characteristics of a parabolic reflector are simulated. The parabolic reflector depth D is varied along with the reflector to detector distance d_{rd} to determine the effect on detected power. The input power is determined from results from Section. 5.5 so that a direct comparison can be made between optical setups later.

The radius of curvature ℓ is kept constant, thus in varying D the aperture A changes. Using Equation. 4.44 and Equation. 4.46, the aperture can be expressed in terms of ℓ.

$$A = 2\ell D \tag{5.1}$$

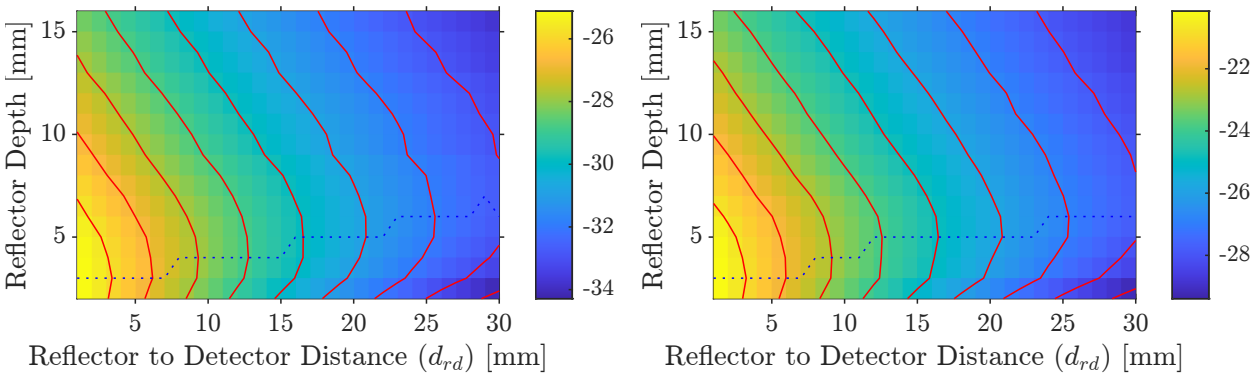

(a) KSLD White (450 nm) (b) KSLD IR (850 nm)

Figure 5.17: Effect of parabolic reflector depth D on detected power versus distance.

Because d is not constant, a smaller reflector depth requires that the detector is closer to the fiber. Without a lens, the parabolic reflector cannot overcome the losses that result from this increased distance to the detector. The best performing parabolic reflector is thus the reflector with a depth of 2 mm which is the minimum possible while still reflecting light from three quarters of fiber.

5.4.3 Elliptical Reflector Depth

The emission characteristics of a elliptical reflector are simulated. The elliptical reflector depth D is varied along with the reflector to detector distance d_{rd} to determine the effect on detected power. The input power is determined from results from Section. 5.5 so that a direct comparison can be made between optical setups.

To contrast the results from the parabolic reflector, the elliptical reflector's radius of curvature ℓ is not kept constant. Instead, the focal length w is swept along with the reflector to detector distance d_{rd} and while the gap g and focal point f are kept constant. For simplicity, the elliptical reflector depth is set to be equal to u, thus $A = v$. Thus the radius of curvature ℓ is given by

$$\ell = \frac{A^2}{D} \tag{5.2}$$

In Figure. 5.18, the elliptical reflector depth is swept. Since D is set to be equivalent to u, the elliptical reflector's focal length being swept along with D. As expected, the maximum

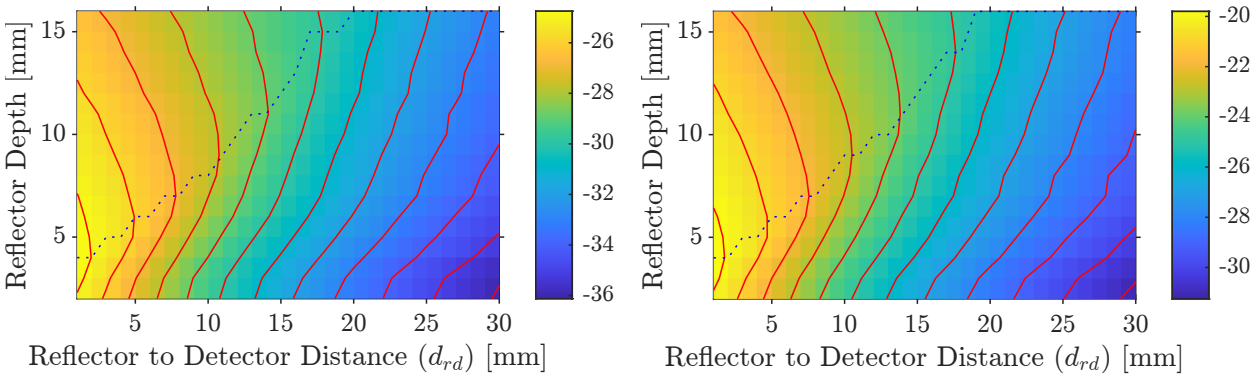

(a) KSLD White (450 nm) (b) KSLD IR (850 nm)

Figure 5.18: Relationship between elliptical reflector depth D and detected power versus distance.

detected power, denoted by the dotted blue line, increases with an almost linear relationship to D as D is coupled to the focal length w.

5.5 Radial Emissions with Added Reflector and Lens

To test the simulation environment's ability to simulate complex systems, the full optical setup is tested. Using the reflector parameters from Figure. 3.3, the simulation model is compared to the experimental results.

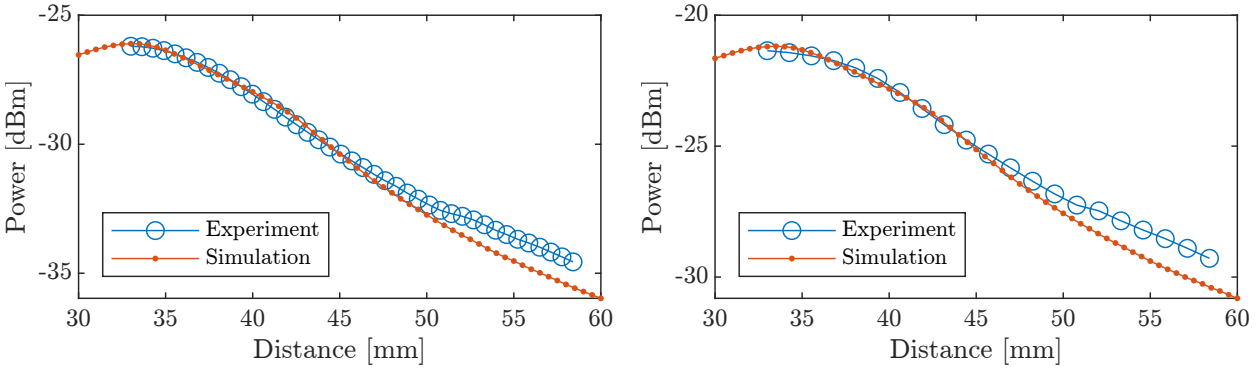

(a) KSLD White (450 nm) (b) KSLD IR (850 nm)

Figure 5.19: Comparison between experimental data and simulation results using a parabolic reflector and condenser lens.

The results of the simulation are compared with the experimental measurements in Figure. 5.19. As no analytical model was made for this system, the offset distance and simulated

detected power are set manually using the difference between smoothing splines fitted to the two trends as an alignment metric.

As the condenser lens can only be used in combination with the spectral filter, a direct comparison between the detected power with and without the condenser lens cannot be made from the experimental data. Qualitatively, the rate of decay in detected power versus distance is similar with both setups losing roughly $3\,\mathrm{dBm\,cm^{-1}}$. The condenser lens does favor small detector surfaces as the power is concentrated to a smaller spot with the use of the lens compared to the uniform power distribution when using only the parabolic reflector.

Overall, the agreement between the experimental and simulation results is strong enough to consider the simulation environment capable of simulating setups of this complexity.

5.5.1 Radius of Curvature

As a potential optimization parameter, the radius of curvature of the parabolic reflector is explored. The source power from Section. 5.5 is used.

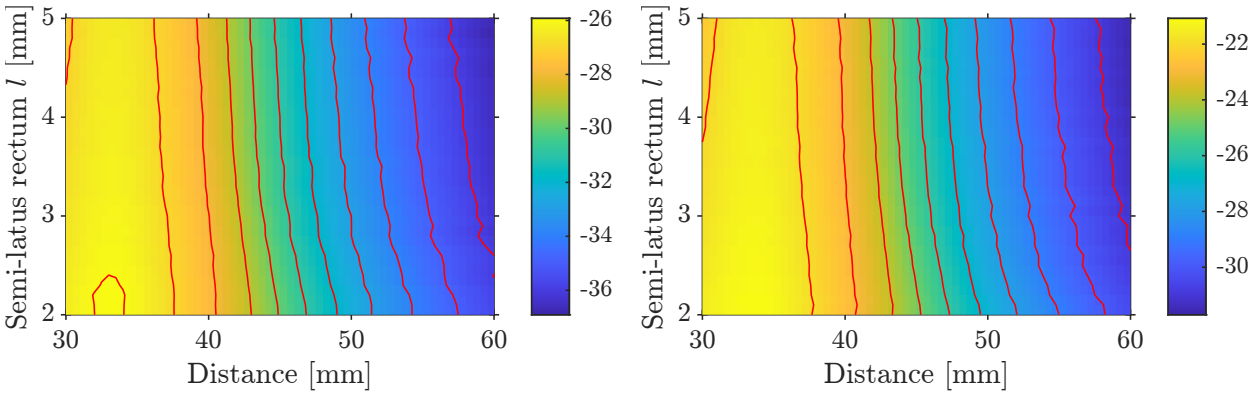

(a) KSLD White (450 nm) (b) KSLD IR (850 nm)

Figure 5.20: Effect of reflector radius of curvature on detected power with the full optics setup.

From Figure. 5.20, the radius of curvature parameter ℓ was swept to demonstrate its effect on the system's performance. The reflector aperture A was modified in conjunction with ℓ to keep the reflector depth D constant. The gap g was also modified to keep the center of the fiber at the focal point of the parabola. The radius of the fiber r was kept constant

at 1 mm and is the reason that the lower bound on ℓ is 2 mm as a gap $g = 0$ requires $f = 1$ therefore by Equation. 4.44, $\ell = 2$.

The same input power used in Figure. 5.19 is used in Figure. 5.20 so that a direct comparison between the setups can be made. It can be seen that a smaller radius of curvature increases the detected power compared to a larger radius of curvature. This is suspected to be because more rays are incident closer to the center of the lens which results in less reflected light as the rays are closer to the normal direction of the lens surface.

5.5.2 Reflector Depth

If the distance between the reflector and the lens d_{rl} needed be changed while the distance between the fiber and the lens was kept constant, the reflector depth would have to be modified. To understand the significance of the reflector to lens distance and the reflector depth parameters, the system is simulated keeping $d_0 + d_{rl}$ constant while varying D.

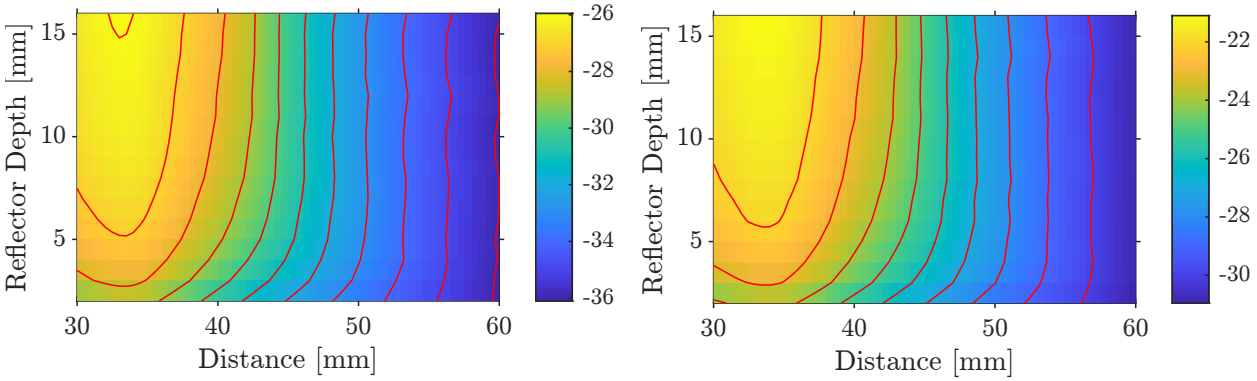

(a) KSLD White (450 nm) (b) KSLD IR (850 nm)

Figure 5.21: Effect of reflector depth on detected power with the full optics setup when $d_0 + d_{rl}$ is constant.

In Figure. 5.21, the reflector depth D is swept to demonstrate its effect on the system's performance. The distance between the reflector and the lens d_{rl} was varied to keep the distance between the fiber center and the lens, $d_0 + d_{rl}$, constant.

The same input power used in Figure. 5.19 is used in Figure. 5.20 so that a direct comparison between the setups can be made. It can be seen that a deeper reflector results

in more detected power when $d_0 + d_{rl}$ is constant. However, there are many scenarios where $d_0 + d_{rl}$ is not constant. The reason a deeper reflector performs better with this constraint is that the percent of light that will not be incident on the reflector or the lens, e.g. the green ray in Figure. 3.4, is smaller for a larger reflector depth. Thus if for an external reason the separation between the fiber and the detector is fixed, the reflector depth should be maximized within the system constraints.

As space is a premium in a rotary interface, reducing the parabolic reflector depth might be deemed beneficial even if it results in a loss of performance. Understanding the relationship between reflector depth D and performance is thus important for balancing these two considerations. In this alternative case, when only d_{rl} is constant, reducing the reflector depth also reduces d_0 and thus the distance between the fiber center and lens is reduced. d_{rl} was set to 2 mm as a reasonable estimate of the gap between the reflector and lens.

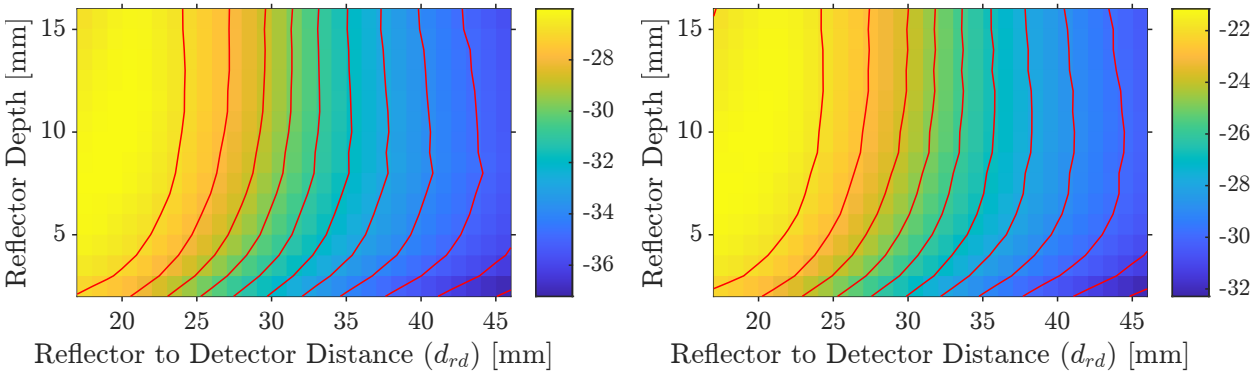

(a) KSLD White (450 nm) (b) KSLD IR (850 nm)

Figure 5.22: Effect of reflector depth on detected power with the full optics setup when d_{rl} is constant. Note, the x-axis is d_{rd} as d is dependent on D.

In Figure. 5.22, the effect of varying the reflector depth D, while keeping only d_{rl} constant, can be seen. Note that the definition of distance is modified from d to d_{ld} as d is dependent on the sweep variable D. As the reflector depth is increased, the detected power is increased with diminishing returns for the largest reflector depths.

This scenario highlights the trade-off between the size of the optical system and the detected power. As the fiber radius r is kept constant, the amount of light that escapes

the system increases with decreasing reflector depth. It may be noted that a small reflector depth will perform better with a smaller fiber radius than a larger fiber radius if its surface is diffusive.

5.6 Aggregate Comparison

The goal of the simulation environment is to enable rapid prototyping of the optical rotary interface. In this vein, understanding which parameters are significant and being able to perform direct comparisons between setups is vital.

5.6.1 Experimental Results

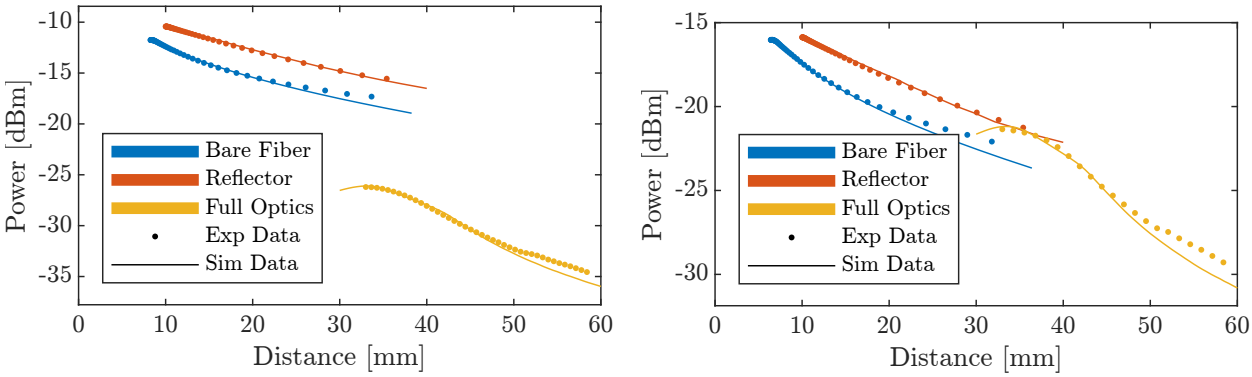

(a) KSLD White (450 nm) (b) KSLD IR (850 nm)

Figure 5.23: Comparison of detected power and simulated results with the bare fiber, the reflector, and the full optics setups.

In Figure. 5.23, results from the bare fiber tests, the parabolic reflector tests, and the full optics tests, are compared. The bare fiber setup consists of only the emissive fiber, the parabolic reflector consists of the emissive fiber and the parabolic reflector, and the full optics setup consists of the emissive fiber, the parabolic reflector, the condenser lens, and the spectral filter. Because of the spectral filter added in the full optics setup, a direct comparison between these results may be misleading.

The amount of power received by the detector is highest with the parabolic reflector for the distances where all three measurements have data. The mean gap between the radial and reflector data is 2.34 ± 0.223 dBm for 450 nm and 1.72 ± 0.211 dBm for 850 nm.

At 850 nm, the full optics performs better relative to the bare fiber and reflector than at 450 nm. This may be due to the broadband nature of the light emitted at 450 nm by the phosphor layer and the fraction of power that is not filtered by the spectral filter. At 850 nm, the phosphor layer is not used and thus the light likely has a narrower spectrum and a higher percent of the light passes through the spectral filter.

5.6.2 Reflector Geometry

The effectiveness of the parabolic reflector and the elliptical reflector is compared when operating without a condenser lens. In this configuration, the elliptical reflector is expected to outperform the parabolic reflector as the elliptical reflector will focus the light to a point instead of focusing it to infinity like the parabolic reflector.

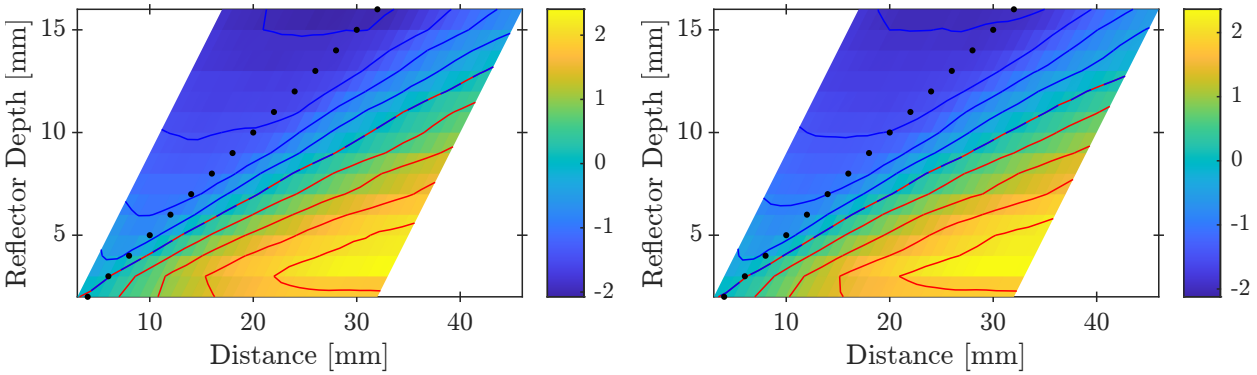

(a) KSLD White (450 nm) (b) KSLD IR (850 nm)

Figure 5.24: Detected power with the parabolic reflector system minus the detected power with the elliptical reflector system.[1]

In Figure. 5.24, the detected power when using the elliptical reflector is subtracted from the detected power when using the parabolic reflector. As an example, a value of -2 dBm indicates that the elliptical reflector system detected 2 dBm more power than the parabolic reflector system for the same reflector depth and distance. Another key difference in the presentation of data in Figure. 5.24 is that the x-axis has been changed from the reflector to detector distance d_{rd} to the fiber center to detector distance d. This allows the size of the

reflector to be taken into account when reviewing its performance.

With these differences in mind, the two different regimes where each reflector excels can be seen. For short distances the elliptical mirror outperforms the parabolic mirror. This is expected as the elliptical reflector's depth D is set to be equal to the focal length of the ellipse w which is denoted by a black dotted line in Figure. 5.24. If $D \neq w$, the performance of the elliptical reflector is expected to exceed that of an equivalently deep parabolic reflector at a distance $d = 2w$.

5.6.3 Collection Optics

The effectiveness of the lens-less elliptical reflector system and the full optics systems with the parabolic reflector and condenser lens are compared. To make this a reasonable comparison, the elliptical reflector distance is measured from the fiber center to the detector, d, while the full optics distance is defined as the fiber center to reflector distance plus the lens the detector distance $d_0 + d_{ld}$. If plotted with the same distance definition, the full optics measurements would be 16 mm further than the elliptical reflector measurements as $d_{rl} = 2\,\text{mm}$ and $d_l = 14\,\text{mm}$ for the full optics setup.

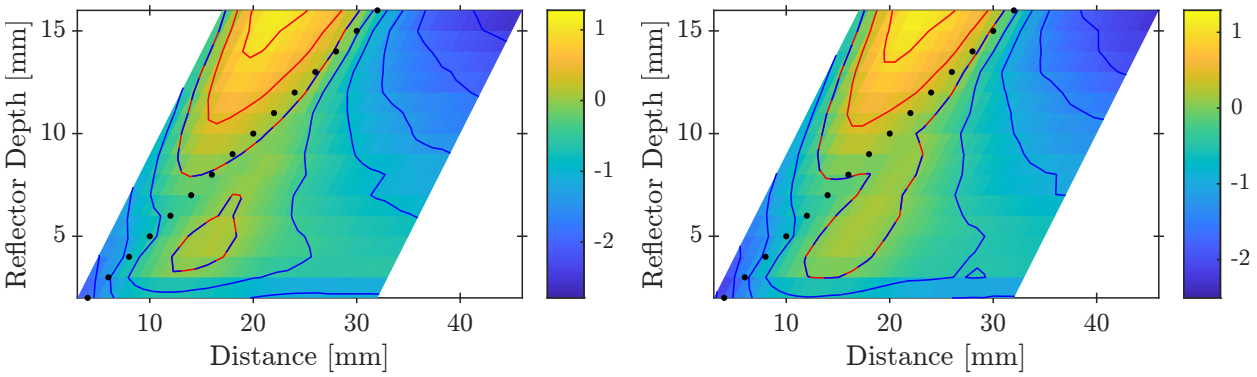

(a) KSLD White (450 nm) (b) KSLD IR (850 nm)

Figure 5.25: Detected power with the full optics system minus the detected power with the elliptical reflector system[2].

In Figure. 5.25, the detected power from the elliptical reflector system is subtracted from

[1]Note that the contours at levels less than 0 dBm are colored blue, the contour at 0 dBm is blue and red, and the contours at levels above 0 dBm are colored red. The contours are placed 0.5 dBm apart.

the detected power from the full optics system.

For $D < 8\,\text{mm}$, the performance of the elliptical reflector setup at the focus exceeds that of the full optics setup by 1.67 dBm and 1.77 dBm for 450 nm and 850 nm respectively. At the full optics setup's best, it beats the elliptical reflector setup by 0.18 dBm and 0.35 dBm for 450 nm and 850 nm respectively.

If we take into account the additional 14 mm that is required for the full optics setup to function, the performance at any reflector depth favors the elliptical reflector setup. The only scenario where the full optics setup is better is when the distance between the reflector and the detector is highly variable as the parallel rays from the parabolic reflector should spread less.

A final detail to note is that the elliptical reflector setup performs best with small reflector depths. This is ideal for a system with space constraints, however a smaller focal length usually results in more divergent rays thus the distance range at which peak performance is reached will be more narrow. It follows that the focal length must be matched with the tolerance on the distance between the reflector and detector.

[2]Contours at levels less than 0 dBm are colored blue, the contour at 0 dBm is blue and red, and contours at levels above 0 dBm are colored red. Contours are placed 0.5 dBm apart. The black doted line is the focal point of the elliptical mirror.

Conclusion

The development of an optical rotary interface using an emissive fiber is presented in two parts. In the first part, performance of a demonstration unit is shown. In the second part, a simulation architecture is developed to speed up further prototyping and optimization.

6.1 Signal Processing

Real valued OFDM using adaptive bit and power loading is implemented on a demonstrator unit. Training symbol assisted and pilot assisted channel estimation and compensation are utilized to optimize the system performance. The training symbol assisted channel estimation is used to compute the subcarrier SNR which is used in conjunction with the SNR vs BER relation to produce bit and power loading maps.

The data rate for a constant BER target and radial distance to the fiber is found at two distances along the length. Inversely, the BER is measured for a constant data rate at three radial distances from the fiber. The maximum achieved data rate is 1018.6 Mbit/s with a BER of 2.7×10^{-3}.

6.2 Simulation Architecture

Through calibration, the methodology for translating physical results into the simulation environment is established. Core characteristics of the emissive fiber system are determined such as the attenuation coefficient and source power. Comparison between available manufacturer listed values and measured values were used to verify the measurement accuracy.

Using an analytical model, the radial emission characteristics were translated into the simulation environment. Qualitative characteristics were verified such as the effect of the fiber radius and the required simulation detail required to accurately replicate experimental results. The complexity of the system was then increased with the addition of a parabolic

reflector and later a condenser lens, the simulation accuracy was confirmed using all available data.

With the simulation environment tested, it was then used to generate an extensive exploration of parameters that would otherwise be limited by the experimental setup. Parameters that are important to the development of an optical rotary interface, such as the tolerance on the fiber placement in the reflector and the trade-off between reflector depth and performance were quantified for the parabolic reflector setup. For the setup with the reflector and lens, the radius of curvature of the reflector and reflector depth were explored such that the trade-off between gap size between the rotary interface rings and performance was quantified.

Finally, direct comparisons between the experimental setups could be performed and demonstrated how the optical rotary interface could potentially be improved by over 2 dB when compared to the current system by switching to an elliptical reflector. The relevant parameters for the optimization of the elliptical reflector and its limitations were discussed.

With the simulation architecture verified and its capabilities demonstrated, its use as a tool to enable rapid prototyping and optimization of the optical rotary interface is shown.

Bibliography

[1] Luiz Eduardo Mendes Matheus et al. "Visible Light Communication: Concepts, Applications and Challenges". In: *IEEE Communications Surveys & Tutorials* 21.4 (2019), pp. 3204–3237. DOI: 10.1109/COMST.2019.2913348.

[2] Cheng Chen et al. "Overview and Performance Evaluation of Wi-Fi 7". In: *IEEE Communications Standards Magazine* 6.2 (2022), pp. 12–18. DOI: 10.1109/MCOMSTD.0001.2100082.

[3] Glenn Dorsey and Michael O'Brien. *Fiber Optic Rotary Joints (FORJ). Performance and Application Highlights*. White Paper. Moog, 2019, MS3324.

[4] Man-On Pun, Michele Morelli, and C-C Jay Kuo. *Multi-Carrier Techniques for Broadband Wireless Communications*. Imperial College Press, 2007. DOI: 10.1142/p530.

[5] Zixian Wei et al. "Multi-user high-speed QAM-OFDMA visible light communication system using a 75-μm single layer quantum dot micro-LED". In: *Opt. Express* 28.12 (June 2020), pp. 18332–18342. DOI: 10.1364/OE.395419.

[6] Mohamed Sufyan Islim and Harald Haas. "Modulation Techniques for Li-Fi". In: *ZTE Communications* 14.2, 29 (2016), p. 29. DOI: 10.3969/j.issn.1673-5188.2016.02.004.

[7] Svilen Dimitrov and Harald Haas. *Principles of LED Light Communications: Towards Networked Li-Fi*. Cambridge University Press, 2015. DOI: 10.1017/CBO9781107278929.

[8] T.M. Schmidl and D.C. Cox. "Robust frequency and timing synchronization for OFDM". In: *IEEE Transactions on Communications* 45.12 (1997), pp. 1613–1621. DOI: 10.1109/26.650240.

[9] Stephen G. Wilson and Rui Shang. *A Modified Schmidl-Cox OFDM Timing Detector*. 2020. arXiv: 2010.00762 [eess.SP].

[10] Dario Pilori. “Discrete-multitone modulation for short distance 100 Gbit/s optical links”. 2015.

[11] Andrea Goldsmith. *Wireless Communications*. Cambridge University Press, 2005. DOI: 10.1017/CBO9780511841224.

[12] A.M. Wyglinski, F. Labeau, and P. Kabal. “Effects of imperfect subcarrier SNR information on adaptive bit loading algorithms for multicarrier systems”. In: *IEEE Global Telecommunications Conference, 2004. GLOBECOM ’04.* Vol. 6. 2004, 3835–3839 Vol.6. DOI: 10.1109/GLOCOM.2004.1379086.

[13] Paul J. Shustack et al. *Photocuring in Areas Where You Typically Cannot Get Light*. Corning Incorporated. URL: https://bit.ly/CorningLDF_pdf.

[14] Eugene Hecht. “Gaussian Laserbeams”. In: *Optics*. Fourth Edition. Addison-Wesley, 2002, pp. 594–596.

[15] C. A. Bennett. “Introduction to Gaussian Beams”. In: *Principles of physical optics*. Wiley, 2008, pp. 372–374.

Copyright

Symbols

Part I

Part II

Glossary